UC Irvine
UC Irvine Electronic Theses and Dissertations

Title

Thermal Radiation Control through Micro-pyramid Texturing

Permalink

https://escholarship.org/uc/item/8rw9x8h1

Author

Sullivan, Jonathan

Publication Date

2020

Copyright Information

Peer reviewed|Thesis/dissertation

UNIVERSITY OF CALIFORNIA
IRVINE

Thermal Radiation Control through Micro-pyramid Texturing

THESIS

Submitted in partial satisfaction of the requirements
for the degree of

MASTER OF SCIENCE

In Mechanical and Aerospace Engineering

By

Jonathan Sullivan

Thesis Committee:
Professor Jaeho Lee, Chair
Professor Yun Wang
Professor Manuel Gamero

Table of Contents

List of Figures

iii

Nomenclature

EM	Electromagnetic (Electromagnetic Spectrum)
E	Energy/Electric Field
H	Magnetic Field
D	Displacement Field
f	Frequency
λ	Wavelength
n	Refractive index
v	Light velocity in medium
$\bar{n}$	Complex refractive index
k	Extinction coefficient
PV	Photovoltaic
TPV	Thermophotovoltaic
PDMS	Polydimethylsiloxane
PETE	Photon-enhanced Thermionic Emission
VIS	Visible light spectrum
UV	Ultra-Violet light spectrum
IR	Infrared light spectrum
NIR	Near-Infrared light spectrum
MIR	Mid-Infrared light spectrum
FDTD	Finite-difference Time-Domain
ε	Emissivity (or Permittivity function, as specified)
α	Absorptivity
θ	Angle of incidence (deg)
R	Reflection/Reflectivity
T	Transmission/Transmissivity
X_{span}	Base dimension of pyramid
Z_{span}	Height of pyramid

C	Cost function
FOM	Figure of Merit, $1 - C$
PML	Perfectly matched layer
T	Temperature (K)
I_{BB}	Blackbody spectral irradiance
$I_{AM1.5}$	Solar spectral irradiance for an airmass of 1.5
P_{solar}	Maximum available Solar power (W/m^2)
$P_{absorbed}$	Absorbed Solar power (W/m^2)
$P_{emitted}$	Emitted thermal power (W/m^2)
$P_{max,emission}$	Maximum amount of power available to emit based on surface T
AR	Aspect ratio

Constants

c	Speed of Light	2.998×10^8 m/s
h	Planck's constant	6.626×10^{-34} J s
k	Boltzmann Constant	1.38×10^{-23} J/K

Abstract of the Thesis

Thermal Radiation Control through Micro-pyramid Texturing

By

Jonathan Sullivan

Master in Science in Mechanical and Aerospace Engineering

University of California, Irvine, 2020

Professor Jaeho Lee, Chair

While selective emitter designs can enable passive thermal solutions for cooling and heating, many selective emitters depend on complex structures, multiple layers, and/or limited application materials. Here we present a general algorithmic optimization framework for the design of single-material 3-dimensional anti-reflective surfaces for radiative thermal management. We use Finite-difference Time-domain simulations in conjunction with a minimization algorithm to computationally investigate optimum passive heating and cooling designs. Based upon a pyramidal topography and depending upon the selected material, our analysis yields that geometric optimization can result in broad set of solutions that significantly enhance spectral absorptivity and/or emissivity. Our findings show that the key mechanism driving the enhancement is the formation of spectrally selective anti-reflective behavior that results from light confinement and localized resonance. This behavior is strongly dependent upon the aspect ratio of the surface features, with higher aspect ratio structures generally leading to a higher spectral emissivity. Applying an optimized surface topology to nickel reduces the normally high metallic visible/near-infrared (IR) reflectivity to the point that it demonstrates a near perfect absorption spectra that ranges from 0.95 – 0.99. Simultaneously, the same geometry maintains an IR-reflectivity below 0.2-0.3, leading to almost ideal thermal passive heating. Conversely, structuring classically

emissive materials such as alumina and Polydimethylsiloxane (PDMS) can further minimize reflection in the IR. This results in a significant enhancement to the IR-emissivity and, subsequently, the cooling performance. These findings will both guide future designs for robust and easily adaptable selective emitter designs and provide a general algorithmic framework for the thermal optimization of geometrically derived optical materials for radiative thermal management.

Introduction

Spectral Radiation

Electromagnetic (EM) radiation is the transmission of energy via the waves of an electromagnetic field that propagates through space regardless of medium[1]. The energy of the electromagnetic wave depends upon the oscillation frequency of the wave; this relation can be described by Planck's equation $E = hf$, where the energy of the wave is proportional to the frequency and Planck's constant (h). This relation can also be visualized in the form of wavelength—where wavelength is related to frequency by the speed of light, $\lambda = c/f$— as the wavelength decreases, the energy of the wave increases. This creates an electromagnetic spectrum that ranges from highly energic waves such as Gamma-rays and X-rays (< 1 pm and 10 pm – 10 nm respectively) to radio waves (cm and beyond).

As governed by Planck's law of radiation, a black body in thermal equilibrium will radiate a spectral distribution of energy dependent upon both the surface temperature and spectral properties of the surface[2]. Thermal radiation – the transfer of heat via radiation – from a surface or body can be described as a function of its Planck distribution (Appendix A). The sun, with a surface temperature near 5800 K, has a spectral distribution that occurs in the visible ($\lambda = 400 – 800$ nm) and near-infrared ($\lambda = 800 – 2500$ nm) regions of the EM spectrum. Most terrestrial bodies at ambient temperature (near 300 K) have a spectral distribution that is in the mid-infrared ($\lambda_{peak} = \sim 9.5$ um). As emission and absorption usually occur at different wavelength bands, spectrally dependent emission/absorption properties are very important to the thermal response of a material.

The spectral properties of a material – and how that material will respond to electromagnetic radiation at a given wavelength – are dependent upon a host of factors, but is primarily controlled by the material's refractive index. Refractive index can be simply thought of

as the ratio of the speed of light to the speed of light in the material, $n = \frac{c}{v}$. The complex refractive index, $\bar{n} = n + ik$ accounts for the dispersion and attenuation of the electric field in the material by adding an imaginary coefficient k, otherwise referred to as the extinction coefficient of a material. Whereas classically electrically conductive materials such as metals are generally reflective due to high values for both the extinction coefficient and refractive index, dielectric materials are transmissive due to a characteristically low extinction coefficient. On a fundamental level, the refractive index describes the microscopic interaction of the electromagnetic oscillation with the atoms of the material and the charge disturbance generated in the atomic structure[3]. As electromagnetic radiation is a wave phenomenon, however, geometric parameters and surface topology can induce localized resonances, confinement, and near-field effects that, in conjunction with refractive index, can control how electromagnetic radiation interacts with a material.

The combination of tunable spectral properties with temperature dependent spectral emission allows for the engineering of materials that control the emission and absorption of thermal radiation. Referred to as "selective emitters", this class of material is a nano/microstructured material that is spectrally optimized for preferential thermal control. Broadly speaking, selective emitter designs can be engineered to optimize the radiative thermal heat transfer of a material. Further, radiative heat transfer is a passive process that does not require any energy input. This allows for unique thermal solutions that minimize unnecessary cost, energy input, or control over a surface. Additionally, for applications where radiation is either the dominant or the only mode of heat transfer, such as spacecraft cooling, high-temperature cooling, PEM thermal management[4], or systems reliant on thermal absorption, optimizing the spectral emission of a material is imperative for system level thermal management or system operation.

Outline of Research

Chapter 1 examines the existing selective emitter and optical-thermal metamaterial designs in literature, with a review of spectral control for radiative heating and cooling applications. Chapter 2 presents an adaptive thermal solution based on pyramidal topology, its usage in previous literature, and rationale for selection. Chapter 3 establishes the computational methods used to predict spectral characteristics and the algorithmic framework, cost functions, and thermal analysis utilized to thermally optimize the pyramidal topology for both passive cooling and heating applications. Chapter 4 presents both the computational results a fundamental exploration of the thermal optimization process as applied to pyramidally textured nickel, alumina, and PDMS. Chapter 5 lists current limitations of the present study as well as highlighting future improvements to the scope and scale of the process. Finally, Chapter 6 provides concluding remarks on the algorithmic design process used in this study and how the process can be applied to both other systems and the experimental fabrication of selective emitter designs.

Chapter 1: Literature Overview

In this chapter, the concepts and applications of radiative heating and cooling via selective spectral engineering will be introduced. Additionally, specific solutions in literature for absorbing/emitting surfaces will be discussed with the goal being to demonstrate potential drawbacks to previous studies and to enhance the understanding provided by the present study.

1.1 Radiative Heating and Cooling

Radiative heating and radiative cooling are passive techniques that depend on radiative heat transfer to either heat or cool the surface respectively. In the case of radiative heating, the intent is for the surface to absorb the entirety of incident radiation while minimizing energy lost to IR emission. For radiative cooling, the intent is to provide a surface that rejects incident radiation while maximizing surface emission; this process can even yield surfaces that are able to cool beneath the ambient temperature.

Harnessing solar irradiation to generate energy directly via a photovoltaic conversion is a very well-known and established process[5], but the thermal energy in solar irradiation can also be efficiently used to generate electricity or as a thermal energy source. An example of this is a
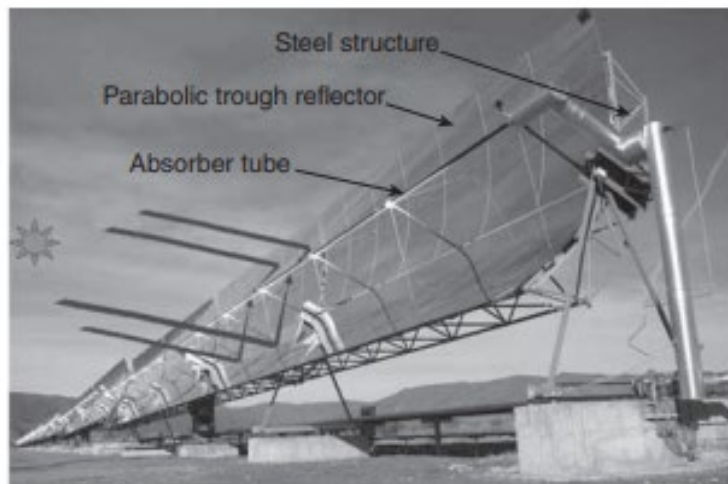

Figure 1. Example of a Parabolic Solar Thermal collector [5]

solar thermal collector (Fig. 1), in which solar irradiation is concentrated onto an absorbing surface and heating a fluid that runs through it [6], [7]. The solar radiation is thus converted into a form useable either by a thermal process or usable as a heat source for a Rankine cycle to produce electricity[7].

Thermophotovoltaic (TPV) and Solar Thermionic devices are other methods that can be used to convert absorbed thermal energy into electricity. TPVs generate electricity in the same way as a photovoltaic (PV) device does– photons of radiation are absorbed and a p/n junction generates an excess electrical charge [8], [9]. The key difference, however, is that while PVs absorb incident solar radiation from the sun (a 5800 K blackbody emitter at a distance of ~ 1.5e8 km) a TPV receives radiation from a surface at a temperature of 1300 – 1800 K at a separation distance of several centimeters. While the power emitted by a body varies by the fourth power of the temperature (Planck's equation), the inverse square law dependence of radiation dominates due to the disparity in distance. This corresponds to an unconcentrated PV system receiving radiation on the order of 0.1 W/cm^2while a TPV receives up to 5 – 30 W/cm^2. Thus, in an ideal case of perfect emission and absorption, the power density of a TPV can greatly exceed that of a PV. Combining both approaches – indirect usage of thermal energy from concentrated sunlight and the quantum conversion of photons to excite electrons – can be combined into what is referred to as a "solar thermionic" device. A key drawback to solar PV generation is that thermalization and absorption of solar energy reduces the available photonic energy available for solar conversion into energy. By combining the PV generation with a secondary waste heat recovery system (thermionic energy converter, TEC) that directly converts waste heat into electricity, the efficiency of the system can be enhanced. Schwede, et. al, proposed a device of this type (Fig. 2) that can operate near ~ 200 °C and has a theoretical conversion efficiency exceeding 50%[10].
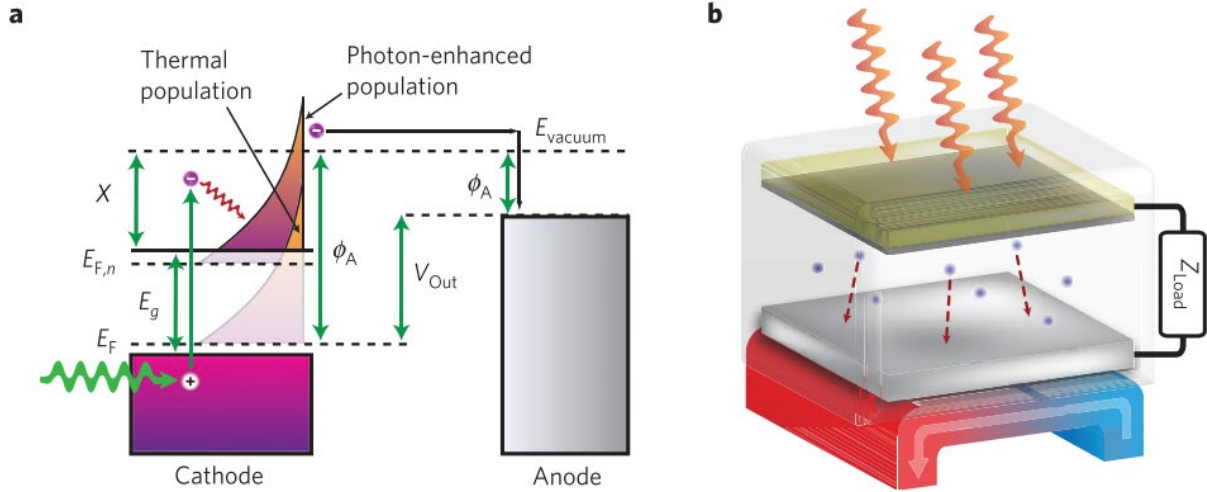
Figure 2. (a) Diagram of PETE process in [9]. The device can harvest both photon and heat energy as a result of photoexcitation. (b) An example of the PETE process in practice. Unused heat energy drives a thermal engine

While radiative energy generation devices depend on the absorption and retention of thermal energy, passive cooling radiators are designed to limit absorbed energy while maximizing thermal energy loss via emission. Specifically, radiative cooling relies on the use of the atmospheric transmission window to emit radiation from the surface into the heat sink of space (~ 3 K). The atmospheric transmission window is a "window" of near unity transmission in the atmosphere from the EM wavelength range of 8 to 14 microns that allows for thermal radiation to be emitted from any terrestrial surface to space through the atmosphere with nearly zero atmospheric impedance [11]. This window corresponds directly to the Planck distribution for a blackbody ~ 300 K. Thus, to properly utilize the overlap between the peak of thermal emission occurring near ~10 microns and the atmospheric window (Fig 3), a surface emissivity should be as close to unity as feasible between 8 to 14 microns for optimal radiative cooling. Simultaneously, the surface must not absorb incident radiation as that will negate any values for cooling achieved by emission in the MIR/IR. This impresses the need for selective emitter designs, as simply utilizing a highly emissive surface will lead to heating when exposed to solar irradiation. Assuming that the surface does not absorb solar radiation, surface emission can lead to significant sub-

ambient cooling ($\sim 7 - 10$ °C) [12], [13]. Interestingly, this process dates back to at least 400 BCE, where Persians formed structures that leveraged the sky window during the cool season to form ice in the desert [14]. In more recent years, the concept of radiative cooling has been applied to reducing building energy costs via surface building coatings, wearable technology for personal cooling, and many other applications.
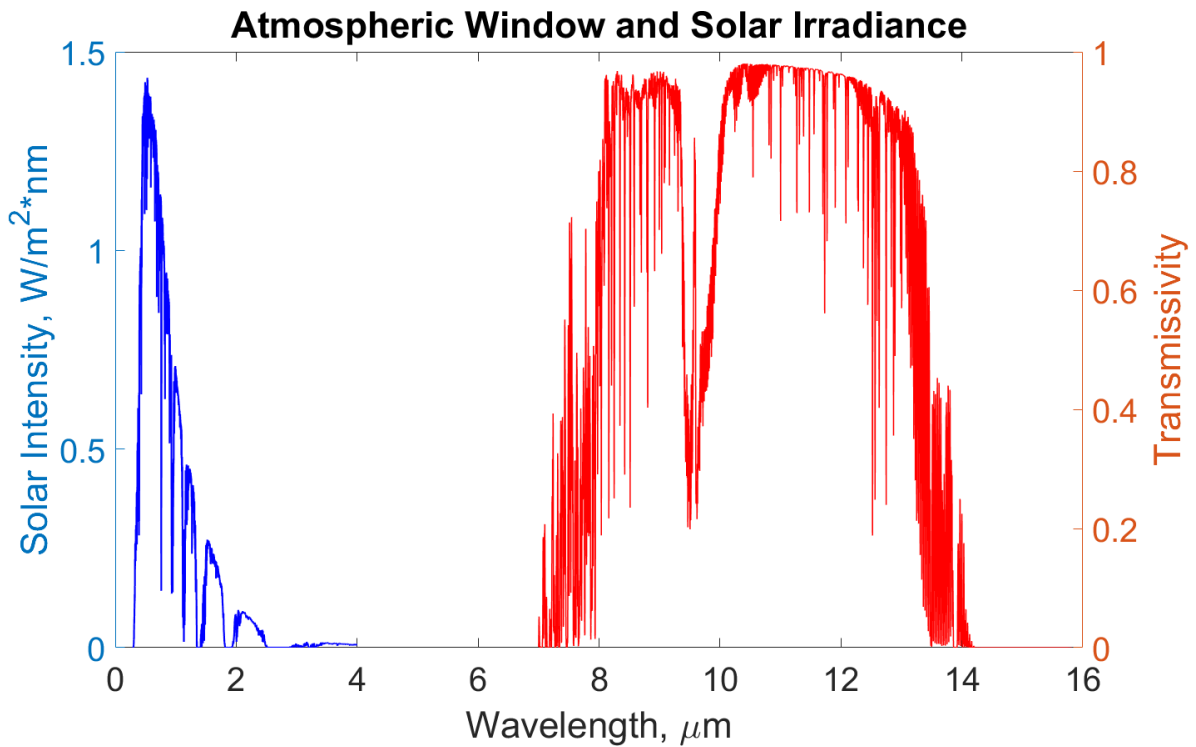
Figure 3. Atmospheric Transmission Window (red) and Solar Irradiance Spectrum (blue). The solar irradiance spectrum plotted is AM1.5, which accounts for irradiance after passing through an "airmass" value of 1.5; this is considered to be the nominal solar distribution for most locations on earth. When integrated it correlates to nearly $\sim 1000 - 1100$ W/m^2 [42]. The atmospheric transmission window occurs between 8 and 14 microns, and allows radiation to pass freely through the atmosphere.

1.2 Absorbing Materials for Radiative Heating Systems

The fundamental element in either a radiative cooling or heating system is in the design of the absorbing or emitting surface. In the case of "radiative heating" systems such as TPVs or solar

thermal collectors, an essential component to maximizing efficiency is utilizing an absorbing material that achieves a near-unity spectral emissivity profile throughout the solar spectrum. In the ideal case, the surface would retain all incident radiation without reflecting any incident radiation or emitting any energy from itself. For TPVs, it is also important that the spectral absorption be maximal for a blackbody distribution matching a nominal TPV temperature between 900 and 1800 °C[8]. Simultaneously, the materials involved must be able to endure high-temperature conditions.

Solutions for absorbing surfaces include many approaches. An approach by Kumar, et. al., [15] is to use a triangularly corrugated surface to enhance solar absorption. As opposed to a planar surface, the corrugated surface has an enhanced absorption profile. Another approach by Selvkumar, et. al. [16], is the use of a multilayer stacked structure of oxide/metal nanofilms (Fig. 4). By combining differing and gradient refractive indices in a sequential form and by combining anti-reflective layers with absorption layers, a structure was designed that can efficiently absorb solar radiation. Multilayer stacked structures generally require specific combinations of both materials and thickness in order to be effective, but are highly spectrally customizable.
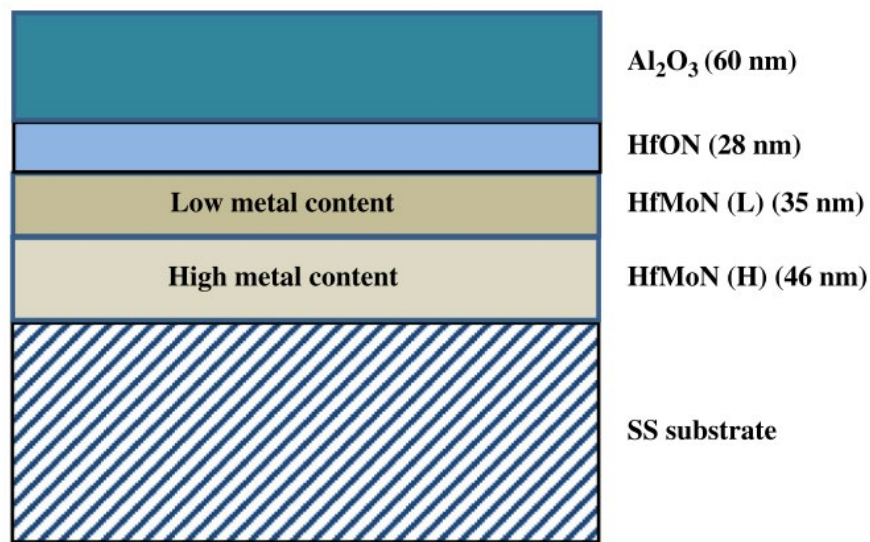
Figure 4. Tandem absorber design proposed by Selvkumar, et. al. [15]. A combination of HfMoN (L and H), HfON, and Al2O3 on a stainless steel substrate

Photonic crystal designs – both 3-D and 2-D – are also used to increase selective absorption properties. Wang, et., al.[17] demonstrated a 2-D "blackhole" cylindrical design that uses a graded refractive index profile to selectively control absorption properties. This generates an "artificial black hole" that effectively absorbs incident waves (of a limited wavelength span) from all directions (Fig. 5). Beyond 2-D photonic crystals, 3-D photonic crystals have also been studied. Qiu, et. al [18] proposed a 3-D photonic crystal design that, similar to a 2-D photonic crystal, has a periodic graduated design for the refractive index that enables omnidirectional absorptive properties.
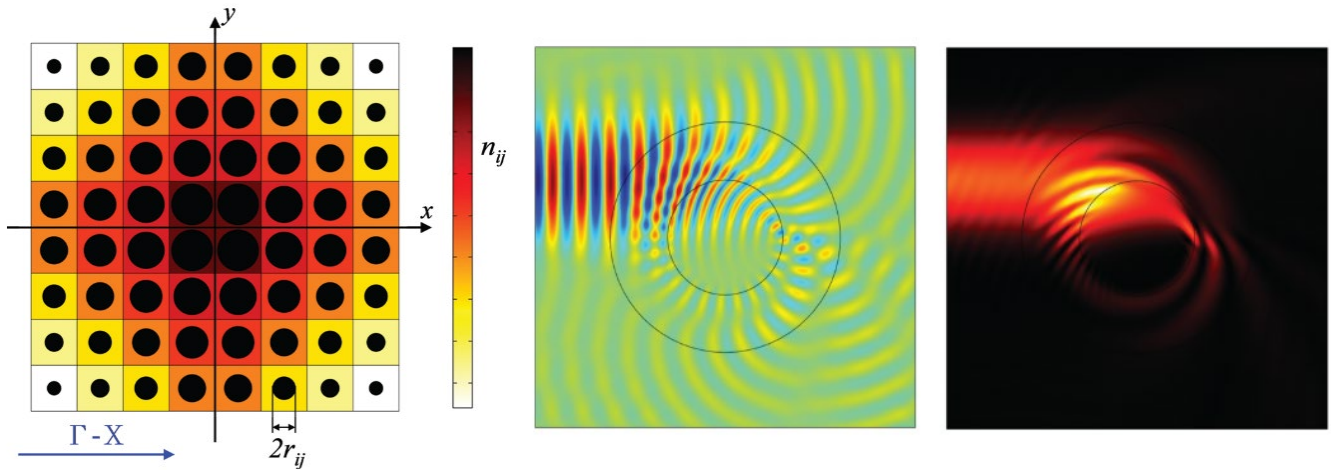
Figure 5. 2-D photonic crystal design in [16]. Left image corresponds to the gradient design of the photonic crystal refractive index. Right images are the electric field distribution and the field intensity patterns respectively.

Engineered nano and microtextured topology is also effective at inducing selective absorption/emission behavior. Zhu, et. al [19] demonstrated a nanodome device (Fig. 6) constructed of hydrogenated amorphous silicon that can absorb ~ 94% of light between the wavelengths of 400–800 nm. This is contrasted to a 65% absorption observed in flat and untextured

devices. Similarly, the "core-shell concept" can be applied to surface topology to selectively modify the absorption/emission properties of the surface. By combining a metallic "core" with a
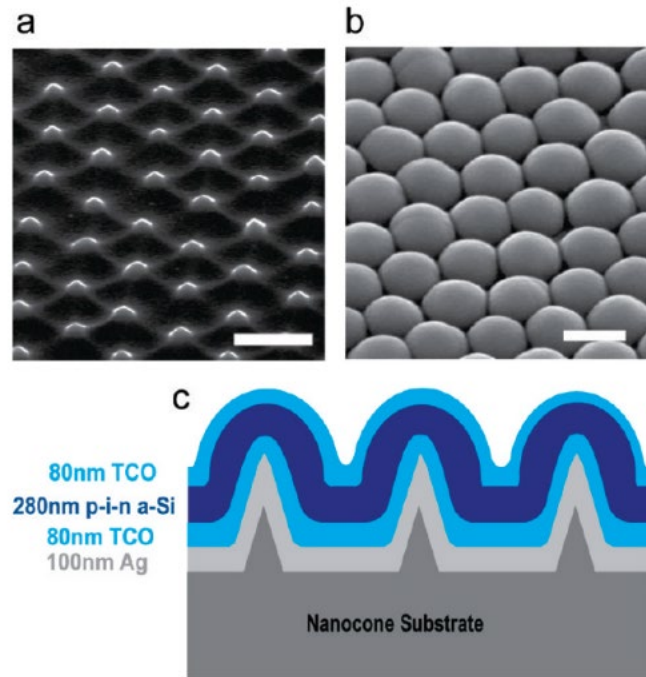
Figure 6. Nanodome a-Si:H cell on a (a) quartz substrate, (b) after deposition of nanofilms, and (c) cross-sectional schematic of device

dielectric "shell", the electric field can be selectively attenuated based on the combination of the refractive index mismatch and the structural geometry. Zhou, et. al [20] and Li, et. al [21], demonstrated significant absorption enhancements via a core-shell design design using Ag/SiO$_2$ and Ni/Al$_2$O$_3$ respectively. Metallic grating structures – such as those proposed by Lee, et. al [22] – can also be used to selectively control the optical band absorption properties of a surface.

1.3 Radiative Cooling Materials

For radiative cooling structures, the surface must be designed such that spectral emissivity is maximal in the thermal emission spectrum while absorptivity in the solar spectrum is kept to a minimum. The thermal emission spectrum is a function of the temperature of the surface, normally peaking in the near-infrared and mid-infrared (NIR/MIR) wavelength regions. The ideal radiative cooler for a body near ~ 300 K has a UV/Vis/NIR absorptivity of zero and emissivity at unity in

the mid-IR. Structures in literature that demonstrate high levels of spectrally engineered radiative cooling performance include similar concepts as the research into solar absorbing materials, but the materials used to create the surface differ due to the necessity of both limiting the solar absorption and maximining the thermal emission. A notable example of the similarity between radiative heating and cooling designs is in the multilayer stack demonstrated by Raman, et. al [23]. The gradient of refractive indices allows for the emission of MIR/IR radiation by employing ceramic materials (SiO_2, HfO_2) that emit strongly in this wavelength band, and the rejection of
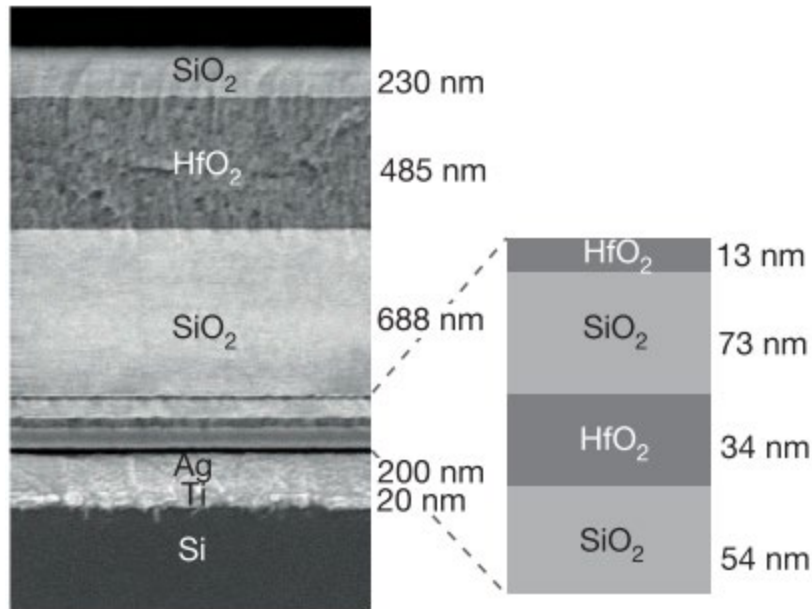
Figure 7. SEM cross-section of structure demonstrated by [22]. Numerical optimization defined the combination of layer thickness and material selection

solar radiation by the reflective Ti/Ag layers at the bottom of the multilayer stack. As opposed to the metallic tandem absorber proposed by [15], the oxide layers are transmissive to visible light and thus absorption of solar irradiation is kept to a minimum.

Polymers are also a well-studied material for radiative cooling applications. This is due to polymers such as Polydimethylsiloxane (PDMS) being nearly completely transmissive in the visible and nearly perfectly emissive in the MIR/IR as a function of their hydrocarbon chemistry.

Recent studies have focused on providing methods to enhance the native absorption while reflecting the incident solar radiation after it is transmitted through the polymer layer. Two such methods include providing a combination of SiO2 (glass) beads in the polymer matrix with a reflective back layer by Zhai, et. al [24] and introducing a high volume fraction of hierarchical hollow glass bubbles into the polymer [25].

Introducing a micro/nanoscale pattern into ceramic materials can also provide an engineered spectral response in the IR. An example of this are nanostructured ceramic "trees" inspired by the morpho butterfly's structural coloration as demonstrated by Krishna, et. al. [26].

Figure 8. (a) Alumina (ceramic) bio-inspired micro-tree design compared with bare Alumina, and bare Aluminum from [25]. (b,c) are the dimensions and designs utilized for the tree-designs

Chapter 2: Micropyramidal Topology for Spectral Radiative Control

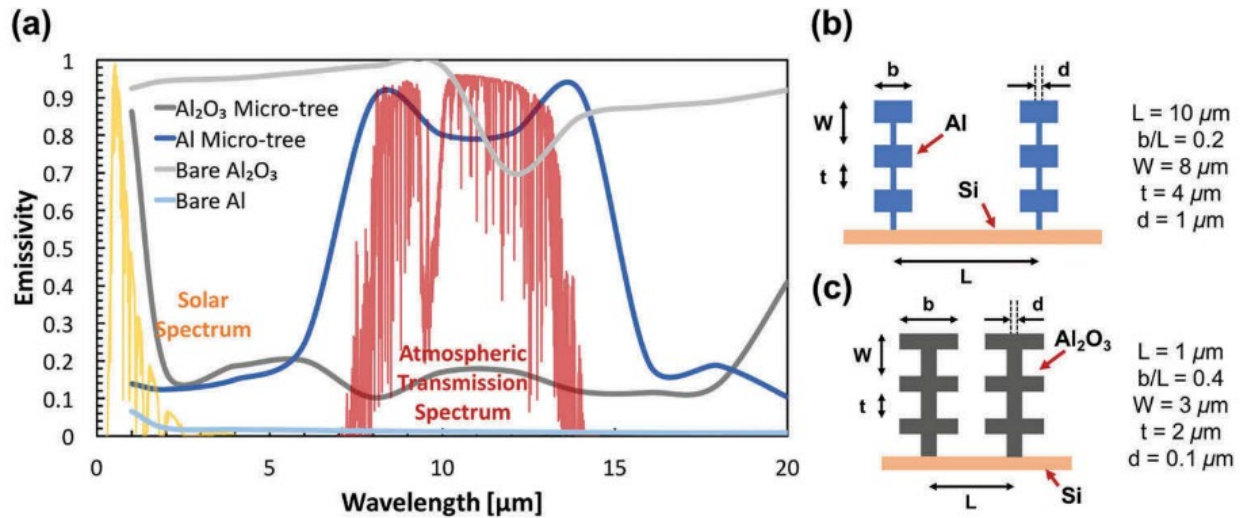While the previous structures for spectral control have yielded excellent results, a way to improve the viability of the solutions shown thus far would be to exploit the anti-reflective behavior of periodic surface topology to provide a generalized topology that can be optimized to match any thermal design requirement. Many topologies can provide spectral control based on geometric parameters, but pyramidal surface structures are selected as the topology due to the extensive tunability of the spectral properties as a function of geometry, as well as pragmatic concerns such as the ease and scalability of manufacture and the array of materials that can be patterned with a pyramidal design. Pyramidal topology is a form of micro/nanoscale texturing that has been studied extensively for optical metamaterials[26, 27]. In previous literature, the anti-reflective properties of pyramidal texturing have been studied primarily as a means of enhancing solar absorption. A notable example of its usage is in the fabrication of pyramidally derived "black silicon" [29], [30]. Liu, et. al.[30] reduced the reflectivity (from 300 to 1200 nm) of untextured silicon from an average weighted value of 34.8% to 11.2% by introducing a microtextured pattern, leading to a more optically black appearance. Li, et. al [21] demonstrated that the anti-reflective behavior of the pyramids can be used to enhance the spectral absorption properties of nickel nanopyramids. To further optimize their results, they employed a core-shell approach, utilizing a thin ceramic layer (Al_2O_3) to further enhance the absorption profile. Based on this work, Peng, et. al.[31] developed nickel pyramidal layers that were deposited on polystyrene films to serve both as an absorption enhancement mechanism and protective layer for solar cells. While these results demonstrate the anti-reflective properties of optical absorbing materials, they are limited by the experimental constraints employed by their process and the fixed relations between the two

geometric parameters of the pyramids. Further, little attention has been paid to non-visible/NIR absorbing materials and the impact of geometry on the thermal transport in the IR for cooling applications.

2.1 Optics of the Micropyramidal Structure

The underlying principle of the anti-reflective behavior relies on the confinement of light within the structure as induced by the geometry. This is a size-effect driven process that is dependent upon two factors; the geometric design and the material(s) refractive index. To exemplify the importance of size on the outcome, it can be shown that pyramidal geometries with a period near to the optical wavelength (400 – 600 nm) are most optimal for the absorption of visible light [28]. The introduction of the pyramidal geometry enables the structure to reflect light multiple times, resulting in an increased optical path length and increasing the probability that the pyramidal structure absorbs the incident EM radiation[28], [31], [32]. In the case where a ray approximation can be used (when $\lambda \ll \Lambda$), the influence of the geometry can be easily visualized in Fig. 9(a). In the case when the wavelength is larger or comparable to the structure (when $\lambda \gg \Lambda$), the geometry can be visualized as inducing a gradient in the electric permittivity function (or
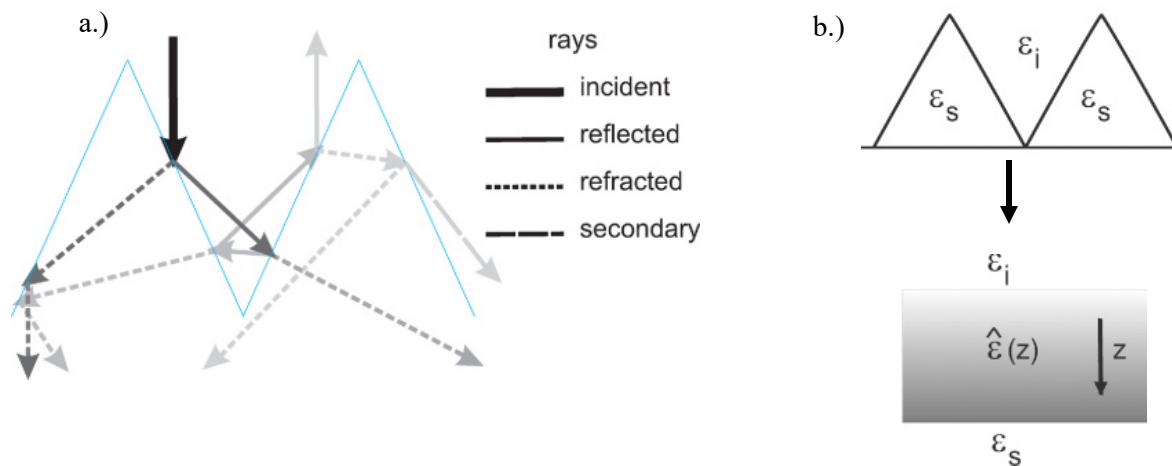
Figure 9. (a) Ray-approximation showing ray propagation in a pyramidal geometry - color intensity corresponds to ray intensity. (b) Visualization of the gradient in the permittivity function [27]

14

the refractive index), as seen in Fig. 9b. The influence of refractive index can be thought of as a fundamental limitation of geometric influence on spectral optical properties. Materials will have wavelength regions where geometric structuring can determine properties, but anti-reflective properties will have a minimal influence over a transmissive material, or a material where the refractive index is much greater than that of the surrounding medium (air, n = 1).

2.2 Experimental Fabrication and Benefits of Pyramidal Topology

While this work does not discuss experimental results, a benefit to pyramidal topology is that it is easily manufacturable and scalable[21] and can be patterned into a wide variety of materials via the template stripping technique[33], [34]. Typical fabrication begins with a chemical etching process to create a template, or mold, from a Si wafer[21], [30]. Periodic micropyramidal topology requires a mask process, but un-uniform/aperiodic micropyramids can also be fabricated using a semi-random process[29], [31] . Due to the fact that both of these processes are performed with a chemical etchant, they are both easily scalable for large-scale applications. Once fabricated,
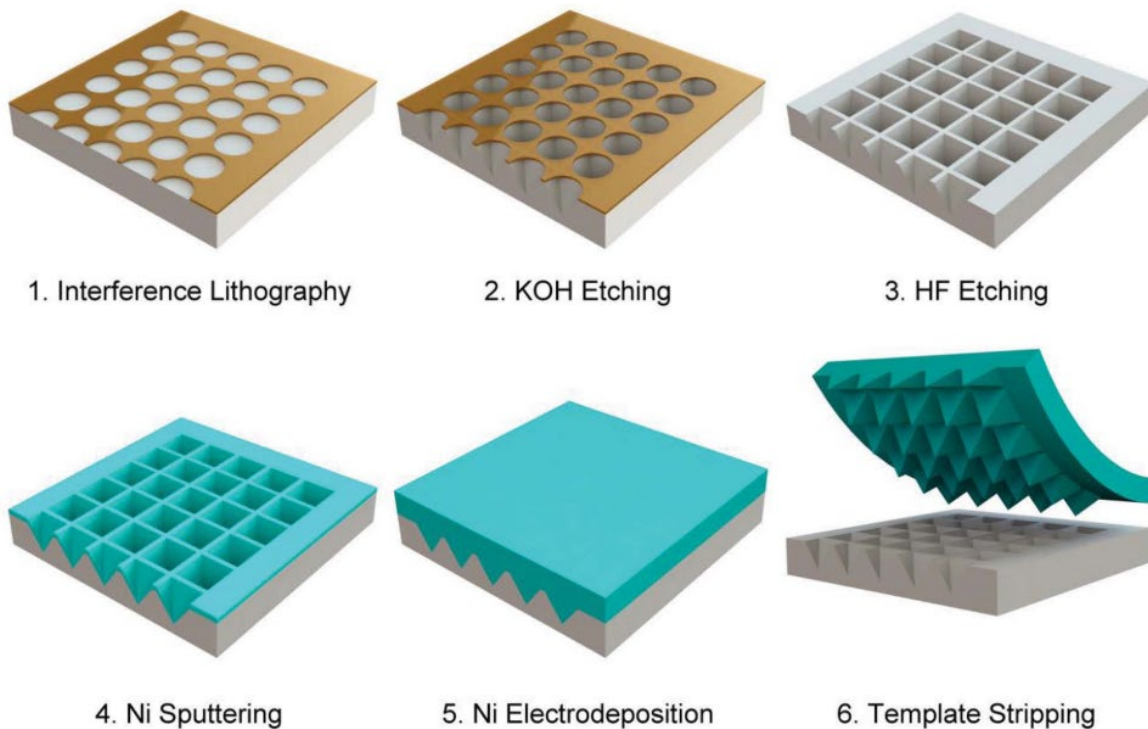
Figure 10. Process utilized by [20] to create periodic patterned nickel films

15

template-stripping techniques (such as Fig. 10) can be used to pattern another material in the "inverse" of the mold geometry. For metal deposition, commonly available electrodeposition techniques can be used to make a patterned metal film without damaging the mold. For materials that cannot be easily peeled, such as a ceramic, a 'sacrificial' mold stage would be required.

An additional benefit to pyramidal topology is that it has demonstrated self-cleaning and hydrophobic properties[30]. These properties make optical coatings configured from micropyramids attractive for many applications due to the reduction in required maintenance and oversight.

Chapter 3: Computational and Thermal Optimization Methodology

Beginning with a micropyramidal pattern, the study will demonstrate how a micropyramidal pattern can be geometrically optimized to provide either radiative heating or cooling in different materials. In this chapter, the simulation framework to compute the surface emissivity and the thermal optimization algorithm are presented.

A generalized form of the structure utilized in the simulation and optimization process is depicted in Figure 11. The illustration demonstrates both the periodicity of the design and the details of the 3D pyramidal unit cell simulated. The key geometric parameters of the unit cell are

Figure 11. Graphic depiction of Pyramidal Unit Cell used in simulations, including a generalized range of dimensions employed.

specified by the span of the pyramid's base and its height (x_{span} and z_{span} respectively). The case that is considered is where the structure'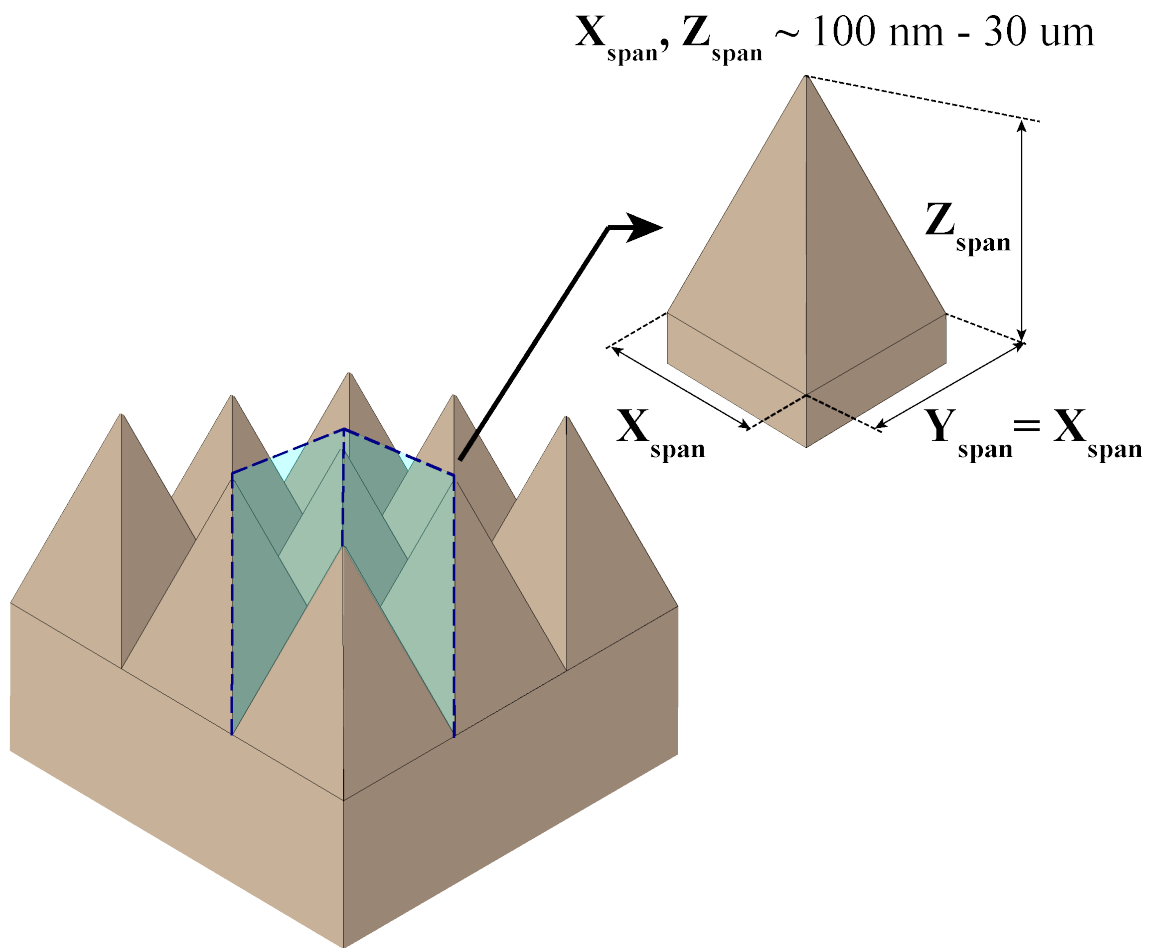s base is symmetric, so x_{span} is equal to the span along the y-axis (y_{span}). The "gap" distance between the edges of adjacent pyramids – which would be a consequence of typical fabrication techniques for periodic microstructures – is not considered in this analysis. The substrate thickness (t_{sub}) is set such that transmission through the simulation domain is negligible and thus this value varies with the chosen material.

3.1 Simulation Framework

Numerical simulations in this work are conducted using Lumerical's commercially available 2-D/3-D finite-difference time-domain (FDTD) solver. The FDTD method discretizes a volume via a mesh and provides exact 3-D solutions for Maxwell's equations for non-magnetic materials. Specifically, the FDTD method solves Maxwell's curl equations:

$$\frac{\partial \vec{D}}{\partial t} = \nabla \times \vec{H} \tag{1}$$

$$\vec{D} = \varepsilon_0 \varepsilon_r(\omega) \, \vec{E}(\omega) \tag{2}$$

$$\frac{\partial \vec{H}}{\partial t} = \frac{1}{\mu_0} \nabla \times \vec{E} \tag{3}$$

Where H, E, and D are the magnetic, electric, and displacement fields, respectively, while $\varepsilon_r(\omega)$ is the complex relative dielectric constant[35]. These equations are solved on a discrete spatial and temporal grid, providing results for the electric and magnetic field in a material, ultimately including both dispersion and absorption[36], [37].

The simulations utilize the unit cell depicted in Fig. 11 in conjunction with periodic boundary conditions in both the x and y-directions to simulate a semi-infinite surface microstructure on the x-y plane. Perfectly matched layers (PML) are used at the top and bottom of the simulation domain to prevent boundary reflection. A plane wave source is used for both normal

incidence (Polar Angle, θ) and angular incidence simulations, but in the case of an angular injection angle, BFAST/Bloch periodic boundary conditions replace the periodic boundary conditions. Frequency-domain field and power monitors are positioned both above the plane wave source and above the bottom PML to monitor the reflection (R) and transmission (T) respectively. The structure's spectral emission can be calculated from $\varepsilon = 1 - R - T$, assuming Kirchhoff's law ($\alpha = \varepsilon$) is valid. For completely opaque structures, the computation of emissivity reduces to $\varepsilon = 1 - R$, but due to the negligible extinction coefficient (k) of both alumina and PDMS within the visible and NIR regions, we use both R and T in the calculation of spectral emissivity.

3.2 Thermal Optimization Framework and Thermal Analysis

To find material geometry configurations that provide optimal results for a variety of different material types, a constrained minimization algorithm is employed to drive the numerical simulations. As will be noted in the results section, although parametrically driven geometric parameters can yield reasonably optimized solution sets, the constrained minimization approach can result in more optimal geometric parameters in a much shorter timeframe. This is especially
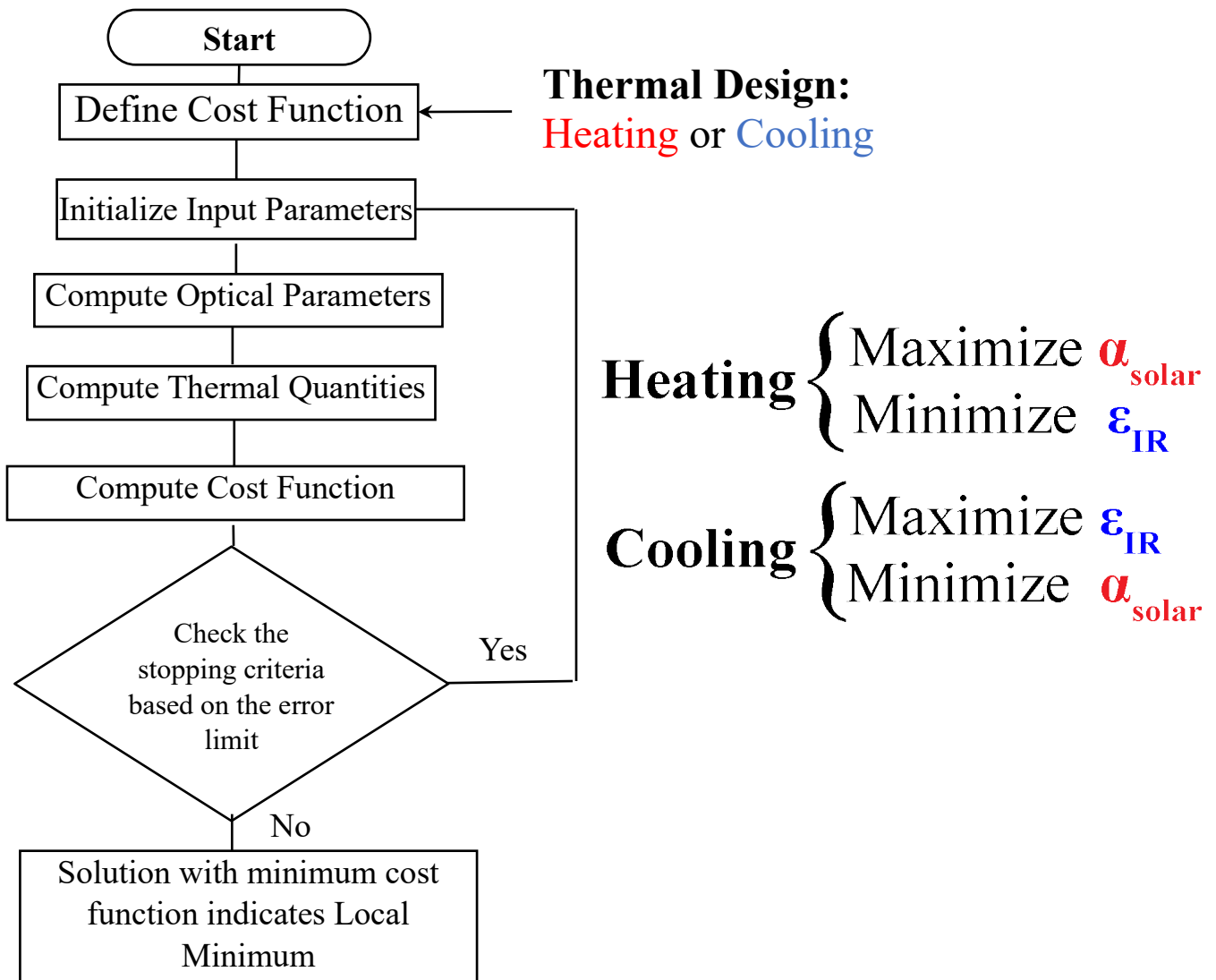

Figure 12. Thermal Optimization Design Loop. Input cost function is determined by the required function of the structure (cooling or heating). The optical and thermal response of the structure are optimized by optimizing the geometric input parameters.

true for more complex geometric designs with more optimization parameters, as parametric optimization becomes increasingly impractical as the design space grows. In this study, the goal is a generalized algorithmic framework for optimizing pyramidal microstructures, so only two parameters (x_{span} and z_{span}) are optimized. The method itself, however, can easily be extrapolated to thermally optimize materials that feature nanotexturing, multilayer structures, coating(s), complex geometry, etc.

As seen in Fig. 12, the optimization process can be divided into several major parts: the objection function (cost function), design factors, and the minimization function itself. The first part of the process is the selection of the objective function. The objective function serves as a mathematical quantification of a design's thermal performance for the chosen application. Thus, the selection of the objective function is determined by the goal of the optimization: namely, a material can be topographically optimized to provide either maximal thermal radiative cooling or optimum absorption of incident thermal radiation. The spectral region(s) that are influenced by pyramidal geometry are determined by the material's properties, as will be observed in the computational results. The cost function is also formulated such that it works in conjunction with the minimization function. For both heating and cooling applications, the cost function has been designed such that in the ideal scenario the constituent thermal terms cancel and the objective function value becomes 0. In the instance of heating, the thermal goal is minimizing the amount of heat lost in the IR while maximizing the amount of incident radiation absorbed[21]. We define the objective function for this scenario to be generally defined by the heat transfer balance of,

$$C = \frac{P_{solar} - P_{absorbed} + P_{emitted}}{P_{solar}} \tag{4}$$

We define this more rigorously as,

$$C = \frac{\int_{\lambda_{min}}^{\lambda_{max}} I_{AM1.5}(\lambda)d\lambda - \int_{\lambda_{min}}^{\lambda_{max}} \varepsilon(\lambda)I_{AM1.5}(\lambda)d\lambda + \int_{\lambda_{min}}^{\lambda_{max}} \varepsilon(\lambda)I_{BB}(\lambda,T)d\lambda}{\int_{\lambda_{min}}^{\lambda_{max}} I_{AM1.5}(\lambda)d\lambda} \tag{5}$$

Where $I_{AM1.5}$ is defined as the solar irradiance for an airmass value of 1.5, I_{BB} is the spectral radiance for a blackbody, and $\varepsilon(\lambda)$ is the spectral emissivity of the surface. The first term is the maximum amount of power that is available for the surface to absorb. For the majority of applications solar irradiation is dominant, so we define the maximum amount of power available to be a function of the solar spectrum. This term is independent of material parameters and can be treated as a constant heat flux. The second and third terms are the amount of incident radiation that is absorbed by the surface and the amount of power emitted by the surface respectively. Atmospheric contributions are neglected in this work, but a term could be inserted into the cost function that accounts for radiative contributions from the ambient environment. The overall system of equations for a radiative heating/cooling surface can be seen in Appendix B. In the ideal case ($\varepsilon = 1$), the surface absorbs all of the available power resulting in the first two terms cancelling. This will not yield C = 0, however, as for the third term to be null, the spectral emissivity must be 0. The entire cost function is normalized by the maximum power available yielding a value for the cost function that is between 0 and 1. Before normalization, the equation has the unit of area independent power, W/m^2.

Conversely, the cost function used in the optimization of radiative cooling surfaces minimizes energy absorbed while maximizing emission. We define the objective function in a similar fashion to the heating case with the heat transfer balance,

$$C = \frac{P_{max,emission} - P_{emission} + P_{absorbed}}{P_{max,emission}} \tag{7}$$

$$C = \frac{\int_{\lambda_{min}}^{\lambda_{max}} I_{BB}(\lambda, T)d\lambda - \int_{\lambda_{min}}^{\lambda_{max}} \varepsilon(\lambda)I_{BB}(\lambda, T)d\lambda + \int_{\lambda_{min}}^{\lambda_{max}} \varepsilon(\lambda)I_{AM1.5}(\lambda)d\lambda}{\int_{\lambda_{min}}^{\lambda_{max}} I_{BB}(\lambda)d\lambda} \qquad (6)$$

The first term is the maximum amount of power that can be emitted by a blackbody for the given temperature, while the second term and third terms are the radiative power emitted and absorbed by the material respectively. In the ideal case, there is no absorption of incident solar irradiation and the emitted power perfectly matches the theoretical blackbody limit for emission. This results in C = 0 for the ideal scenario. Identical to the heating case, C = 0 is not a physical possibility but provides a computationally ideal lower limit that drives the optimization process.

The other two parts of the optimization process depicted in Fig. 12 – the design factors and minimization function – work in tandem. Design parameters (x_{span} and z_{span}) are defined and passed to the simulation domain for each iteration. The output of the simulation— $\varepsilon(x_{span}, z_{span}, \lambda)$—is then used to compute and evaluate the cost function. This process begins with an initial guess for x_{span} and z_{span} ($x_{initial}$ and $z_{initial}$) upon which a baseline value for the cost function is established. The minimization function will then check the cost function when the values for x_{span} and z_{span} are varying combinations of above and below $x_{initial}$ and $z_{initial}$. For this work, fabrication methodology and ease do not constrain the sizing or range of x_{span} and z_{span} and the range is widely constrained with $100\ nm < x_{span}, z_{span} < 40\ \mu m$. Subsequent iterations will continue to test variations of x_{span} and z_{span} until the stopping criteria is reached; this value is based on a predefined error limit. The "optimum" value is the local minimum of the cost function for the combined array of x_{span} and z_{span}.

Chapter 4: Optimization of Micropyramidal Topology for Radiative Heating and Cooling

The results of the algorithmic process are presented below for three materials: nickel, alumina, and PDMS. Nickel is chosen to be optimized as a heating material, due to previous usage in literature as well offering a strong combination of low metallic refractive index with excellent mechanical properties. Alumina and PDMS are chosen for the cooling materials as they are commonly used emissive engineering materials that will be shown to be optically enhanced by the inclusion of an optimized micropyramidal surface topology. In both cases, the roles of geometry, aspect ratio, and size in the determination of optical properties and thermal properties and will be discussed for each material optimization.

4.1 Optimization of Heating Material via Nickel Micropyramids

Planar metallic surfaces are generally poorly absorbing materials – this is due to most metals being conductive and thus featuring a steep complex refractive index curve. Although the characteristically high reflectivity of metals can be reduced by introducing severe oxidation at the surface, we demonstrate that strong absorption within the visible and near-infrared (NIR) regions is possible by microscale geometric patterning of a single metallic material without the need for an oxide coating. Here we choose to optimize nickel as nickel has a complex refractive index that is smaller than the refractive index of metals such as silver or aluminum[38]; this leads to a wider absorption peak in the VIS/NIR and provides a larger margin for geometry to determine optical properties. For the nickel optimization process, we utilize a plane wave source that ranges from 300 nm – 10 μm. We choose this wavelength (λ) span as λ = 300 – 2000 nm is the most relevant region for solar absorption, and due to the high refractive index in the IR, nickel is observed to

asymptotically approach an emissivity near ~ 0.1 near and beyond $\lambda = 10$ µm generally irrespective of the micropattern's x_{span} and z_{span}.

The goal of the optimization process for nickel is to maximize the amount of energy absorbed – particularly in solar relevant wavelength regime of $500 - 1000$ nm – while minimizing the amount of energy lost to emission. As noted previously, the material's intrinsic refractive index places a fundamental limit on the level of influence that geometry can provide over a wide spectral range. For nickel, the absorption enhancement is dominant in the visible and NIR regions, resulting in the material being best suited for optimization as a passive heating material. Fig. 13(a) shows a distribution of geometric designs that result from several iterations of the minimization process when the heating objective function is employed. We define the Figure of Merit (FOM) as FOM when the heating objective function (Eqn. (4) and Eqn. (5)) is employed. We define the Figure of Merit (FOM) as FOM $= 1 - C$, such that the results are more easily visualized. Bare planar nickel is computed to have a FOM of ~ 0.35. This is a result of bare nickel absorbing nearly 38% of incident solar radiation while only losing a fractional quantity of thermal power to emission in the IR. Comparatively, Fig.13(b) demonstrates that even un-optimized surface structuring via micropyramids drastically increases the FOM to $0.6 - 0.7$. This indicates that even unoptimized structures can research a solar absorption efficiency of $60 - 70\%$, representing a 25-35% increase compared to bare nickel.

As can also be observed from Fig. 13(a), the minimization process yields a host of solutions that are quintessentially optimal and have nearly negligible variation in optical performance. The global optimum computed from multiple iterations of the optimization process has a heating FOM of 0.963, which occurs at $x_{span} = 0.65$ µm and $z_{span} = 2.1$ µm. Both the emissivity and reflectivity of this structure can be observed in Fig. 3(b), but the exceptional increase of absorptivity to a value

b.)

a.)
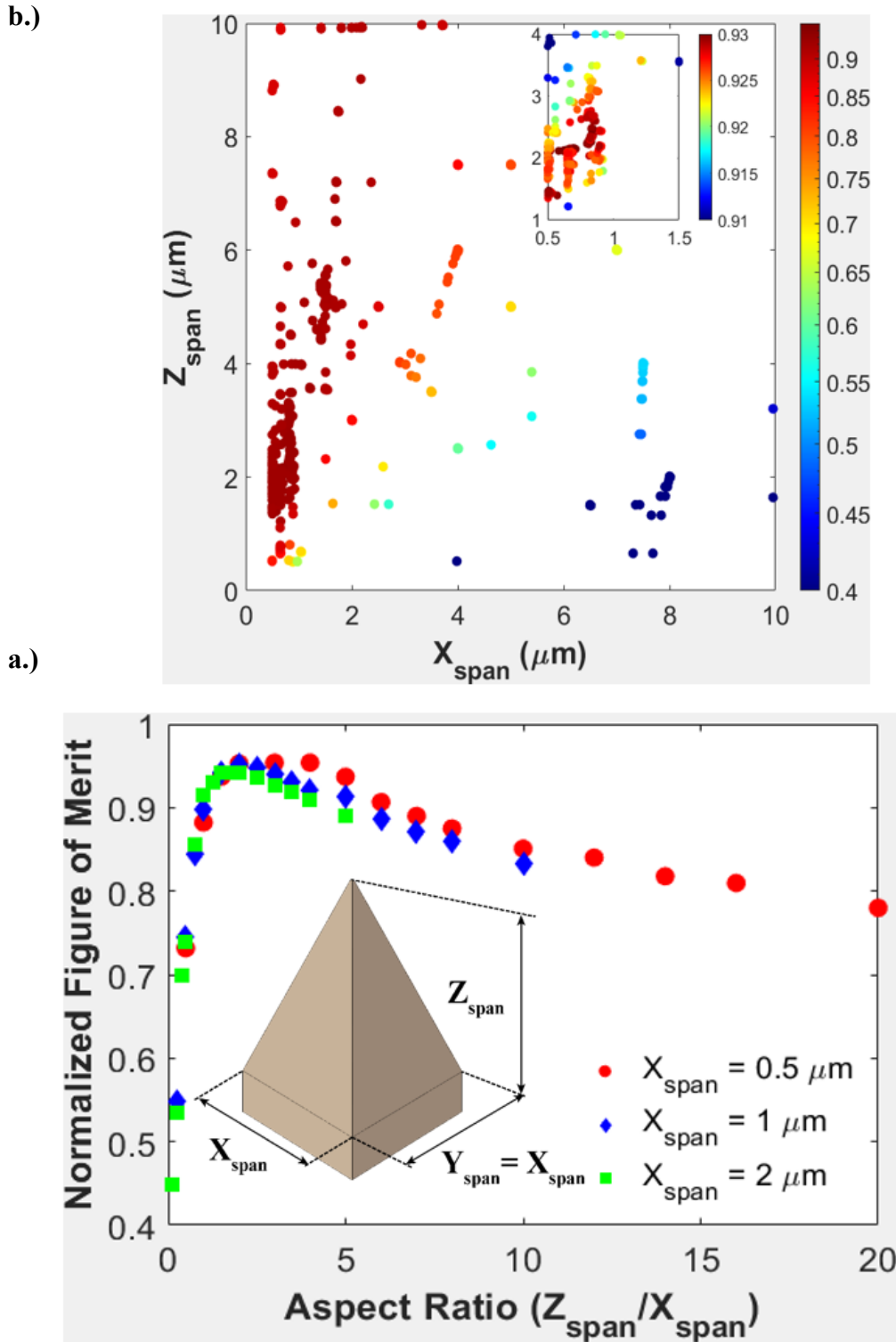
Figure 13. (a) Heatmap of individual geometric combinations as a function of both input geometric parameters (Xspan, Zspan). Color bar is plotted logarithmically to show clear delineation in the Figure of Merit. A large array of nearly equivalently performing geometric parameters are identified, but a selected solution array (inset) shows that there are globally optimum solutions. (b) Normalized Figure of Merit as a function of structural aspect ratio. To maintain proper structural scale, the aspect ratio is normalized by a fixed X/Y span and the Z span is varied.

near $\alpha = 1$ between the wavelengths of $\lambda = 300$ - 2000 nm results in an absorption efficiency of 98.6%. Specifically, this structure can be predicted to absorb 986.6 W out of the available 1000.4 W for AM1.5 between $\lambda = 300$ nm and $\lambda = 10$ μm. Thermal emission leads to a thermal loss of 23.9 W for the optimized structure, which is 19.1% of the maximum blackbody emission between $\lambda = 300$ nm and $\lambda = 10$ μm at 300 K. By comparison, two local optimization minimums occurring at (x_{span} * z_{span}) of 0.51 * 1.45 μm and 0.9 * 1.98 μm have absorption efficiencies of 97.3% and 96.9%. Accordingly, their figures of merit are 0.96 and 0.953 respectively. Although the absorption efficiency decreases by ~1-1.5% for both local optimums when compared to the global optimum, a decrease in thermal emission— 13.8% and 13.7% of the blackbody limit respectively—results in the global optimum having a figure of merit that is only $0.3 - 1\%$ higher than the aforementioned local optimum geometries. Thus, while finding a global optimum using this minimization process requires many iterations, finding a local minimum that has exceptional performance occurs very early in the process and many solutions can reliably reach absorption efficiencies passing 94-96%.

The overall trend in the heating figure of merit can thus be described predominantly as a function of the aspect ratio of the structure. This trend can be observed in Fig.2(b), which plots the figure of merit as a function of the aspect ratio. It is important to note that while the aspect ratio is intrinsically unitless by definition, we choose to define aspect ratio as:

$$Aspect\ Ratio = AR = \frac{Z_{span}}{X_{base}} \tag{5}$$

where X_{base} is constant and used to normalize while Z_{span} is swept in the simulations. While we observe a trend between the aspect ratio and figure of merit, this distinction is made such that the necessity of a nanometer/micrometer scale periodicity is not lost. From Fig.13(b) we conclude

that, based on a X_{base} from 500 nm to 4 μm, increasing Z_{span} will rapidly increase the figure of merit until it reaches a maximal value ~ 0.92 – 0.96 for an aspect ratio near 2.5 - 3. After the local maximum for a X_{base} the FOM will then decrease. This trend can be explained as a function of both the thermal and absorption efficiency increasing until a critical maximum when the absorption efficiency saturates while the thermal emission efficiency continues to increase. At larger ARs, the absorption efficiency decreases while the thermal emission efficiency continues to increase. The trend in Fig.13(b) also makes it evident that experimentally viable solutions using fixed aspect ratio fabrication and template stripping can yield exceptionally efficient radiatively heating materials. For common KOH fabrication methods, etching along the Silicon [1 1 1] plane yields a fixed base angle of 54.3°, resulting in a pyramid with a fixed aspect ratio of 0.857, irrespective of X_{span}. As can be seen in Figure 13a, a FOM of 0.8 – 0.85 is computationally possible for structures that can be readily and reliably fabricated using KOH processing and subsequent template stripping techniques to fabricate nickel thin films. It can also be concluded that while the base dimension has an impact, the driving factor in the enhancement of the absorption efficiency and increase in FOM (decrease in the heating cost function) is the aspect ratio.

The physical phenomenon behind both the influence of aspect ratio as well as the geometry's determination of surface optical properties is the introduction of anti-reflective behavior as a consequence of the structuring. Two geometries are plotted in Fig. 14(a,b) – both the global maximum and a fixed aspect ratio structure (Design I, AR = 0.5) with the same base dimension as the global optimum (Design II, X_{span} = 0.65 μm). As the simulation domain has a near-zero transmission due to the intrinsically high imaginary component of nickel's refractive index, the driving factor behind the emissivity/absorptivity enhancement is the decrease in reflection as a function of the geometry. As seen in Fig.14a, the maximum intensity of electric

28

field for the same wavelength remains contained in the optimized geometry and unconfined by the low-aspect ratio structure. While photons are normally elastically scattered from a metal (conductor's) surface, Fig.14 (a) shows that the introduction of both a cavity and scattering angles by the surface geometry reduces the reflectivity significantly by confining scattered photons inside the morphology. It is evident that the higher aspect ratio structure maintains confinement – and increased absorption – over a much larger wavelength region compared to the low aspect ratio micropyramid texturing. It should be noted that the magnetic field component plays a limited role in the enhancement of the absorption compared to the electric field.

Comparing the two structures in Fig.14, the reduction in reflection can be further seen as an overlap of the complex refractive index curve for nickel and the geometric scale of the nickel micro/nanopyramidal surface topology. For wavelengths beyond the solar spectrum (> 2000 - 3000 nm) the complex refractive index of nickel begins to rapidly rise, which leads to surface morphology having a reduced impact on the optical properties. Fig. 13(b) validates that while increasing the aspect ratio to form very steeply angled structures (AR > 5) can lead to a mildly increased absorption coefficient in the IR-band, it is far more limited in scope than the geometric enhancement available in the visible/NIR. From simulations with other metals such as silver and aluminum we observe that geometric dependent anti-reflective behavior has a far more limited spectral range of influence, predominantly due to the much higher slope in the refractive index for these materials. Additionally, the optimization process yields that the most optimal results have base dimensions near the solar spectrum wavelengths ($X_{span} \sim 500 – 2000$ nm). This result is to be expected as localization and resonance effects as a function of geometry are the most effective when the dimensions of the geometry are either smaller or near to the injection wavelength.
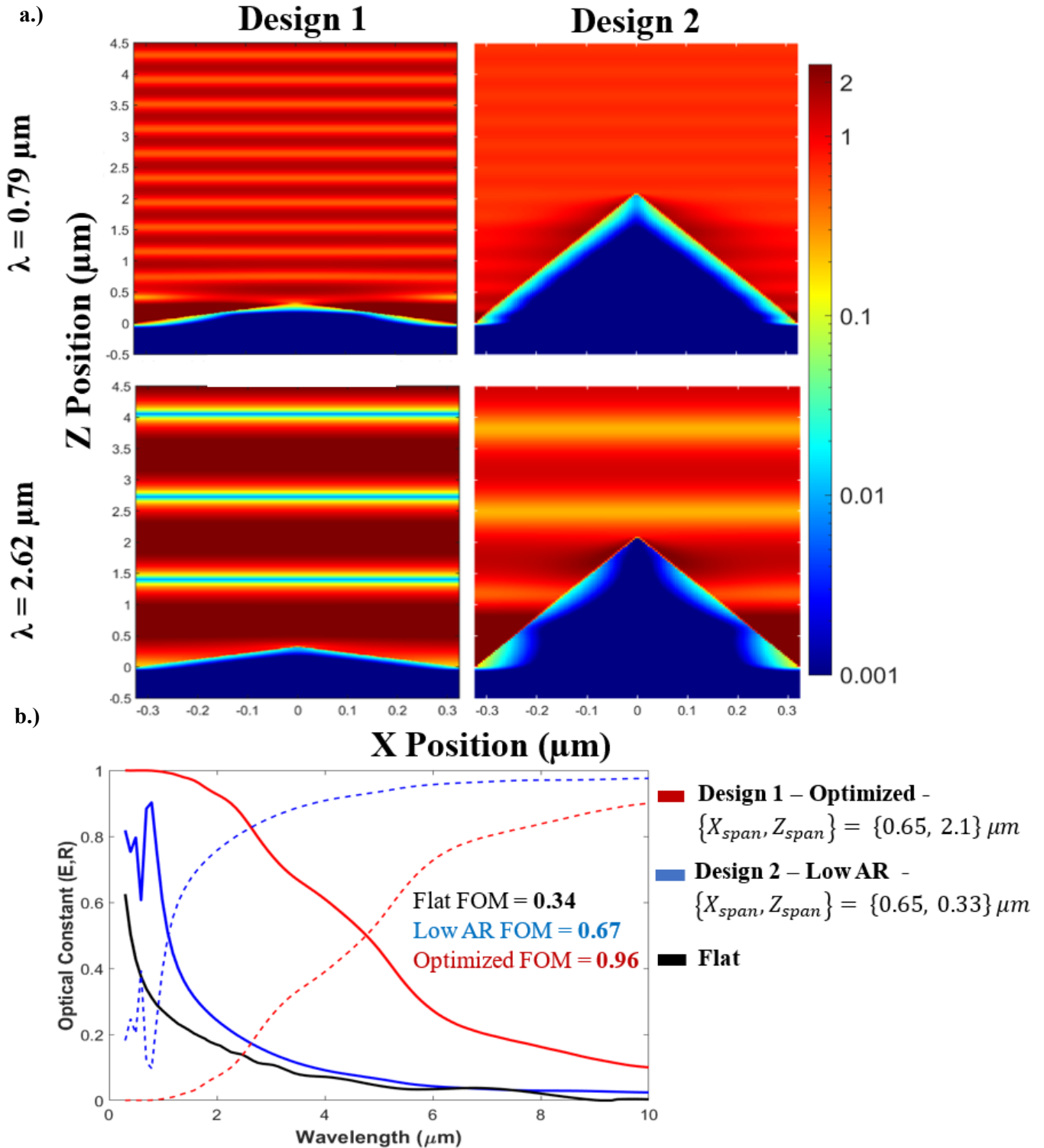
Figure 14. (a) Plotted magnitude of the Electric Field at two selected wavelengths for two distinct designs. Design I is a structure with AR = 0.5, and Design II is the computationally optimized geometry. (b) The computed emissivity of both designs are compared to the computational prediction for a untextured nickel surface.

As discussed previously, the structure being simulated is both symmetric and periodic along both the x and y-axes; while most simulations occur using a 3-dimensional (3-D) FDTD design space, the algorithmic process easily transfers to a 2-dimensional (2-D) design space. Reducing the geometry to 2-D yields a grating structure as the simulation domain assumes the triangular shape (x_{span} and z_{span}) is infinitely extruded along the y-axis. For a plane wave with an injection angle of $\theta = 0°$, there are minimal differences in the absorptivity computed between the 2-D and 3-D domains. Reducing the geometry to 2-D systematically reduces the computational time required for simulation, allowing for far more rapid optimization of the geometric parameters. A significant downside to this simplification, however, is that the 2-D grating has a significantly different absorptivity when the injection angle or azimuthal angle (θ and φ respectively) are not 0°. As shown in Fig. , the 3-D pyramidal geometry has near omni-directional absorption properties that are not observed in the 2-D grating structure.

4.2 Optimization of Micropyramidal Cooing Design using Alumina and PDMS

Although periodic microstructures significantly enhance the spectral absorption of metals in the VIS/NIR, and therefore become excellent solar absorbing materials, they cannot provide optimal passive cooling simply as a function of geometry. As opposed to the conductive properties of metals, ceramic and polymer surfaces (generally) emit well and do not reflect a high percentage of incident radiation. Thus, they are perfect suited for passive cooling applications, where high emission in the mid-IR and low absorption in the VIS/NIR can be combined to form self-cooling materials that can remain below the ambient temperature. The predominant example of passive cooling materials in recent literature are based on polymers that combine naturally high MIR emissivity with VIS/NIR reflectivity. While these materials are already well suited for passive cooling, introducing optimal micropyramidal surface texturing to polymers and ceramics reduces the minimal MIR spectral reflectivity of the surface to near zero, creating almost perfect IR-emitting materials. Here, we choose Alumina[39] (Al2O3) and PDMS[40] as they both common engineering materials and well-studied for passive cooling applications.

For the optimization of both the Alumina and PDMS surfaces, the goal is to maximize the emission in the MIR and minimize VIS/NIR absorption. We choose a wavelength range from 4 – 16 μm for the optimization of both materials. This wavelength span is utilized because the Boltzmann blackbody distribution for a body at 300 K centers near ~10 μm, with over 60% of the total thermal emission possible occurring in this span. Increasing the domain size to account for longer IR wavelengths has diminishing returns as the resources required to simulate the domain increase while the relative gain in available thermal emission decreases. Simultaneously, both materials are highly transmissive in the VIS/NIR region for the thickness required by the simulation to negate MIR transmission (100 μm). Consequently, the VIS/NIR response of the

cooling materials is not a function of geometric optimization, and is instead a function of the substrate. The cost function utilized for optimization, then, is a modified version of the cooling objective function shown in Eqn. (6) and (7), where the solar absorption term is not considered. The simplified version is a function of only the maximal emission, meaning that the surfaces are evaluated based on how closely they approximate the theoretical blackbody distribution. Fig. 4 shows a distribution of results collected from multiple iterations of the optimization process utilizing the modified cooling objective function on alumina. As before with the Nickel optimization, the figure of merit is computed as FOM = 1 – C, such that the results are intuitively visualized. Planar alumina, under this cost function, is computationally evaluated to have a FOM of 0.53— indicating that it emits 53% of the blackbody limit for a surface at 300 K. It is evident from Fig. 4 that, similar to Nickel, the introduction of periodic patterning results in a significant increase in the figure of merit.

The optimization process for alumina produces a host of solutions that are essentially equivalent. The trend is distinctly similar to that of nickel's optimization – increasing the aspect ratio of the structure increases the surface's emissivity until a point of saturation. For alumina, the key difference is that while the emissivity enhancement remains strongly dependent upon the
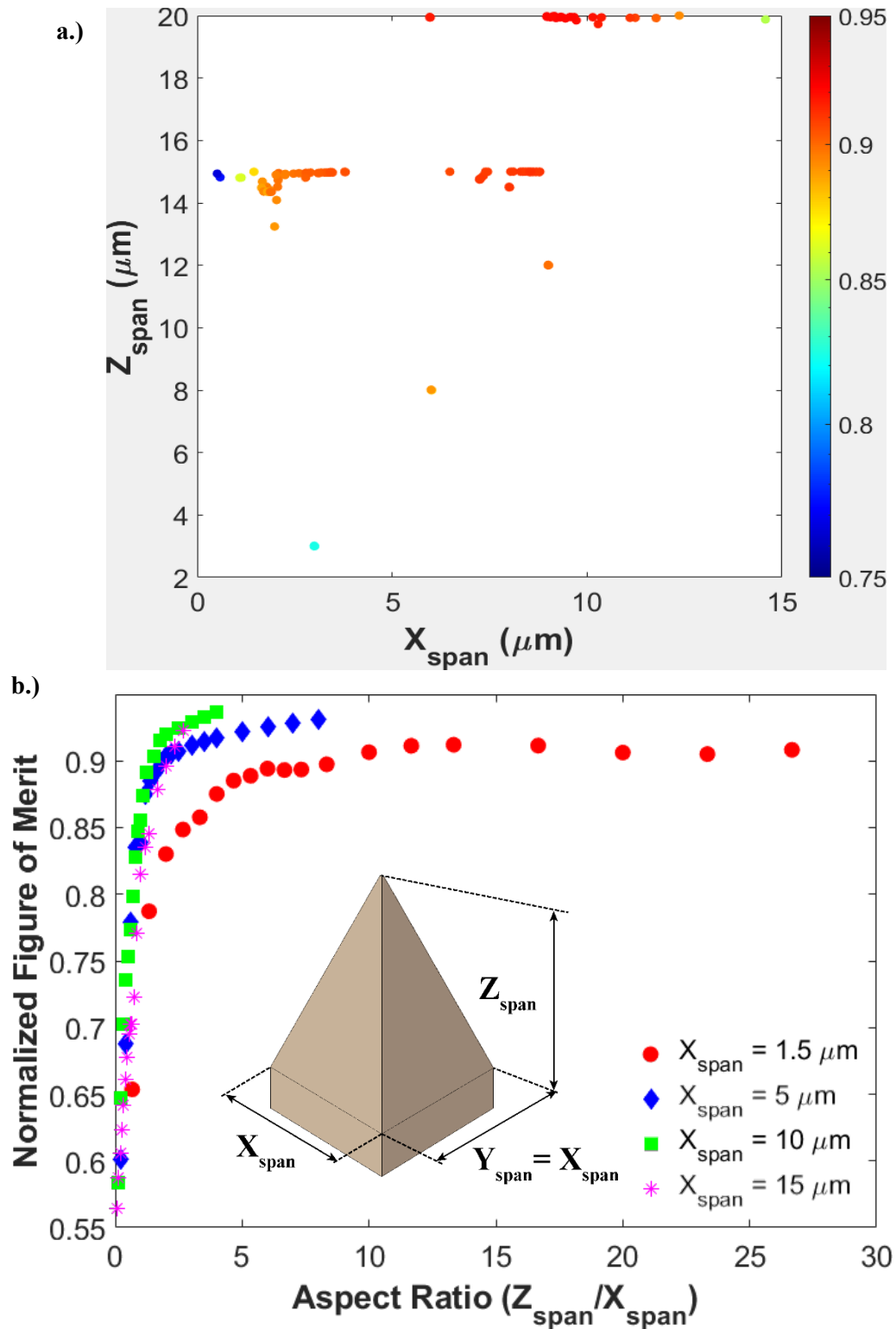
Figure 15. (a) Heatmap of individual geometric combinations as a function of both input geometric parameters (Xspan, Zspan), (b) Normalized Figure of Merit as a function of structural aspect ratio. To maintain proper structural scale, the aspect ratio is normalized by a fixed X/Y span and the Z span is varied.

wherein it is clear that the maximum of the figure of merit increases as the base dimension increases. As opposed to nickel micropyramids, which have an optimal base dimension to be near 500 nm – 1000 nm, alumina micropyramids have a critical base dimension between 5 – 15 µm. When alumina micropyramids are dimensioned beneath this critical range, the maximum figure of merit decreases. This trend makes it difficult to establish a distinct global optimum using this methodology for this material and geometry; the constraints of geometry imposed by computational resources limits the process. For the results shown in Fig. 15b, each structure is simulated a constraint of $z_{span} = 40$ µm. Based on the results shown in Fig 15(a) and (b), however, the near equivalency in thermal emission between structures with AR > 2-5 mitigates the necessity of simulating structures beyond this constraint. The trend in the FOM is to asymptotically approach a maximum FOM that is dependent upon the base dimension for the structure. When $x_{span} = 10$ µm, the FOM approaches ~ 0.95, indicating that the geometry can emit ~95% of the theoretical maximum at 300 K. Comparing $z_{span} = 5$ µm, 10 µm, 20 µm, and 40 µm for a fixed x_{span} of 10 µm, the FOM is 0.753, 0.856, 0.920, and 0.937 respectively (AR = 0.5,1,2,4). This corresponds to an increase in FOM of ~0.22, 0.32, 0.39, and 0.41 when compared to bare alumina. The asymptotic behavior between AR and FOM indicates that while the maximum for a given base dimension might not be observed when the height is constrained, a solution within 1-2% of the maximum is easily achievable. Thus, the optimization of the cooling cost function for alumina quickly yields local minimums beneath 0.1 (FOM = 0.9) but this solution is unlikely to be the global maximum due to the constraints utilized.

The negligible difference between the constrained and unconstrained minimum cost function is a result of a saturation in emissivity. The results plotted Fig. 16 show that the
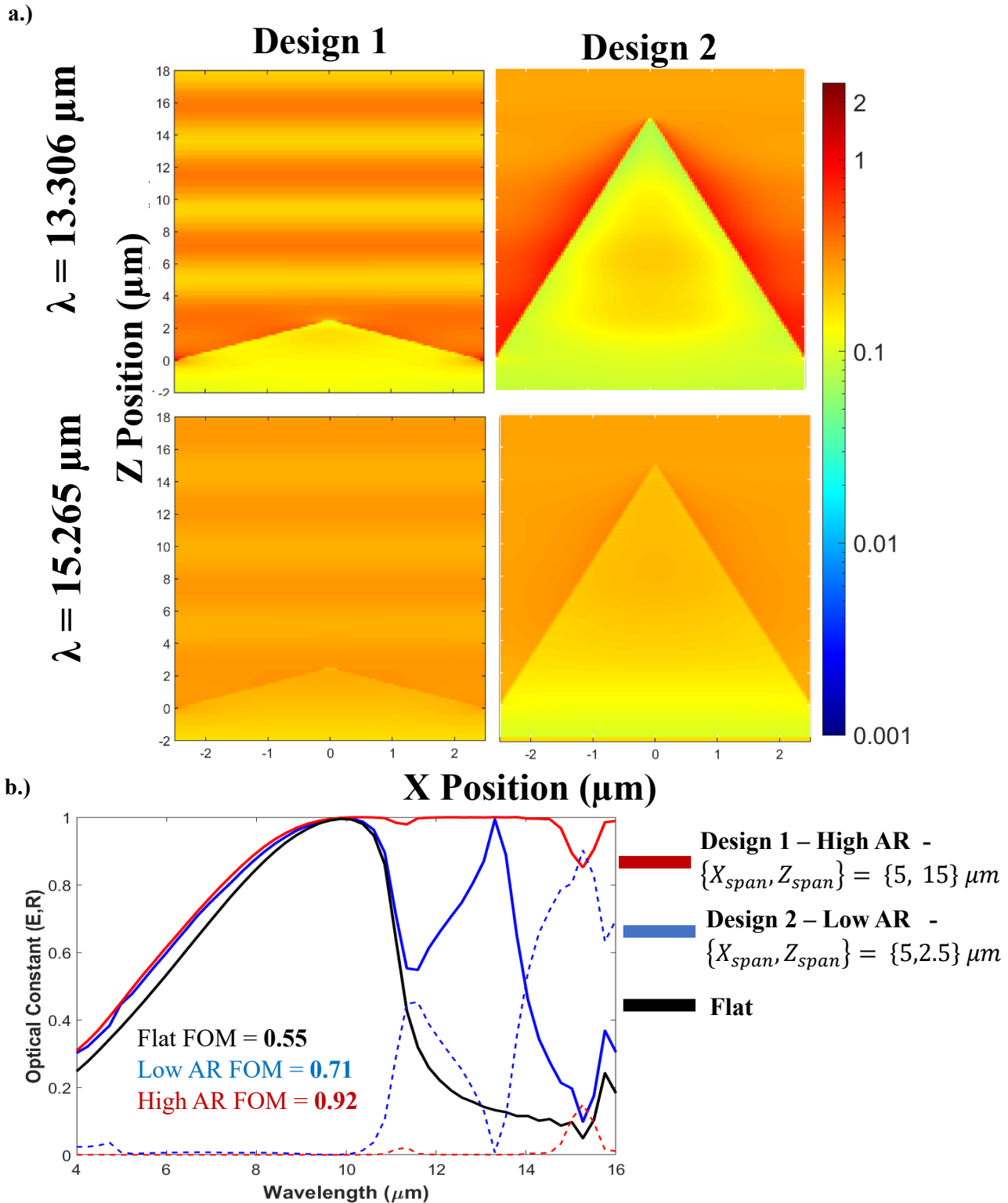
Figure 16. (a) Plotted magnitude of the Electric Field at two selected wavelengths for two distinct designs of Alumina. Design I is a structure with AR = 0.5, and Design II is the computationally optimized geometry. (b) The computed emissivity of both designs are compared to the computational prediction for an untextured Alumina surface.

36

μm. The anti-reflective behavior can again be observed in Fig. 16a to be a function of the containment of the electric field by the geometry. While the wavelength region has shifted to the MIR due to the material properties of alumina, the fundamental behavior remains the same. The efficiency of the anti-reflective behavior is a function of the geometry. However, as the emissivity can only range from 0 to 1, the influence of geometry on the emissivity proportionally decreases as the aspect ratio increases. This phenomenon is seen in Fig. 16b, in which a low aspect ratio (AR = 0.5) and high-aspect ratio (AR = 3.0) geometry are plotted simultaneously. Compared to the bare alumina case, the low-aspect ratio micropyramidal pattern has a drastic effect on the emissivity by significantly decreasing the spectral reflectivity when $\lambda > 10$ μm. For the high-aspect ratio geometry, the emissivity is almost uniformly at unity, but the relative difference between the high and low-aspect ratio structures is much lower than the relative difference between the bare alumina and low-aspect ratio geometry. Thus, as observed previously, many solutions can yield a similar local minimum cost function, and the difference between the local minimum and the global minimum cost function is small.

Although PDMS has an innately high emissivity in the MIR/NIR regions due to its intrinsic refractive index[40], employing the same cooling optimization procedure results in the same anti-reflective trend and subsequent increase in MIR emission that was observed in alumina. The modified equation (4) used for the alumina optimization results in a value of FOM = 0.91 for untextured PDMS. Fig. 17 exemplifies that even minor texturing of a PDMS surface increases the FOM to a value near 1.0, indicating that textured PDMS is a near perfect NIR/MIR emitter when textured. Despite having a characteristically high emissivity, the introduction of micropyramidal texture to the surface reduces the already minimal reflectivity to a value near 0 in
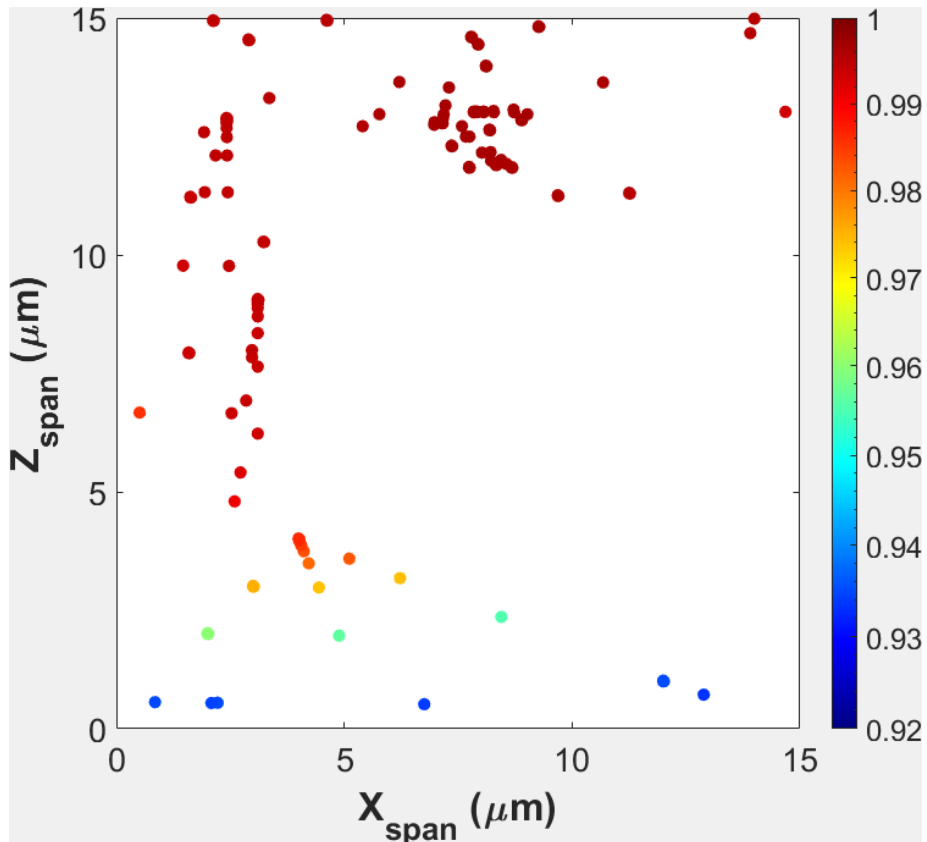
Figure 17. Heatmap of individual geometric combinations as a function of both input geometric parameters (Xspan, Zspan) for PDMS micropyramids

the NIR/MIR. The trend observed in Fig. 17 is that even low-aspect ratio texturing with AR < 1

yields emission efficiencies of 95-96%, with AR > 2 PDMS micropyramids displaying thermal

emission efficiencies at ~99%. This thermal efficiency can be seen in Fig. 18(b), where the

Blackbody distribution (at 300 K) is plotted alongside both the spectral distribution for the

optimized PDMS structure and flat PDMS structure. With minimal deviation, the textured PDMS

surface nearly perfectly matches the theoretical blackbody maximum. This is a result of the

introduction of texturing, as observed in Fig. 18(a), which demonstrates that texturing reduces the

minimal reflection observed in PDMS to a near 0 value and subsequently increases the absorption to near unity.
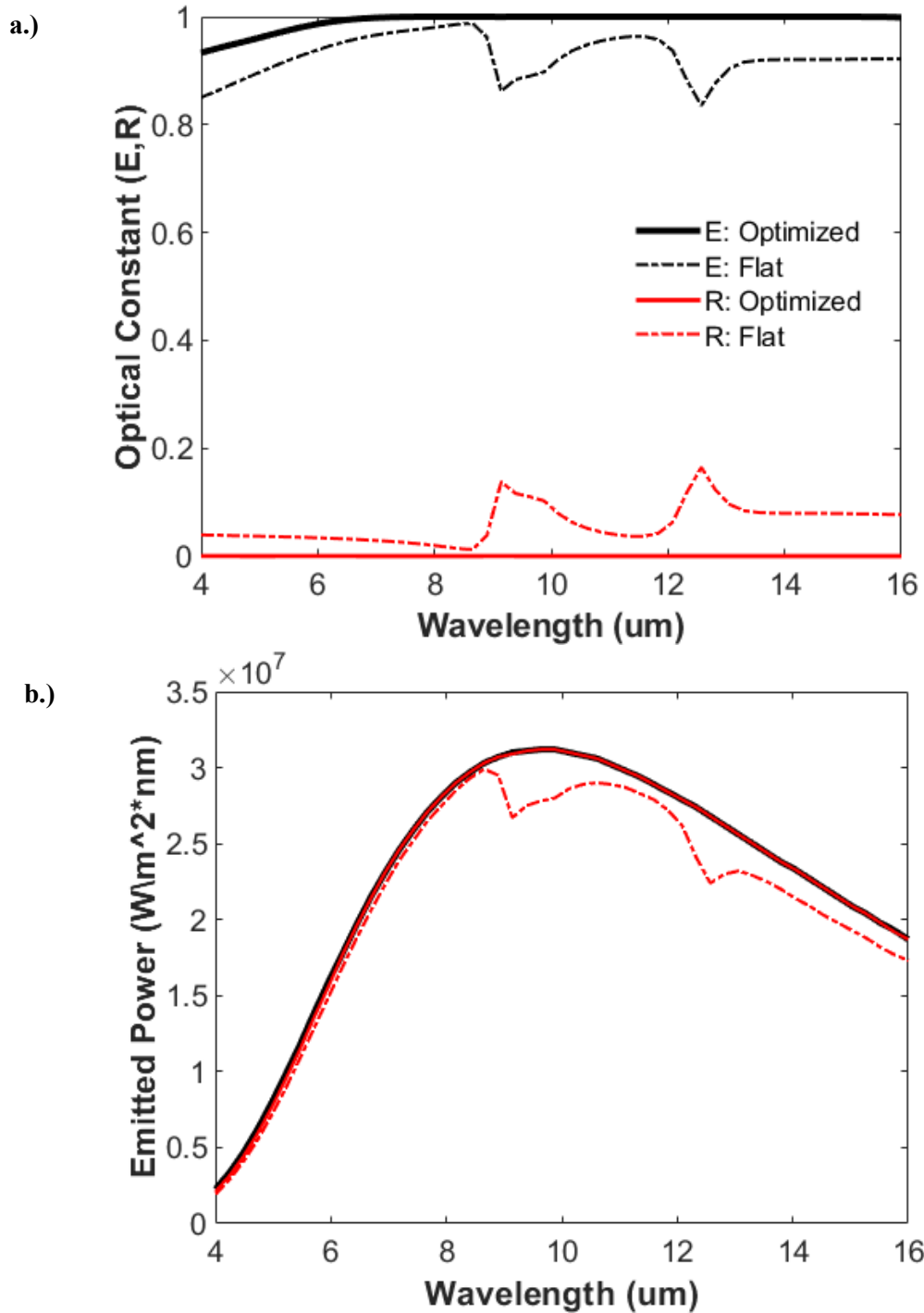
a.)

b.)

Figure 18. (a) Comparison of Flat and Optimized Textures for PDMS. The decrease in reflection induced by the geometry drives the emissivity increase. (b) The Planck distribution for a Blackbody at 300 K (black line) and the Emission spectrum for the Optimized/Flat PDMS textures (Red/Red-dashed respectively)

Chapter 5: Conclusion and Future Work

The work demonstrated by this study comes with several limitations in scope. The key limitation is only three materials were optimized for a single material and geometric configuration. By combining more complicated geometries or topologies – or introducing hierarchical texturing (such as through surface level nanowires) – the optimization domain can grow greatly. Computationally, the method used for optimization – while efficient – can be dramatically improved by introducing methods such as machine learning. The method can be readily adapted to incorporate both more design variables as well as a different driving minimization function, and the incorporation of both of these elements will be the core to future computational research.

Furthermore, another important limitation is that there is currently a lack of experimental results to back the computational results. This is complicated by the nature of the fabrication of the structures, as while it is rudimentary to design periodic structures with a fixed aspect ratio (beginning with a Si mold and a KOH etching process), higher aspect pyramidal structures are not easily scaled using this method. Other less scalable methods would be required to fabricate the geometry as demonstrated in this work. Future work will first focus on the fabrication of the fixed aspect ratio structures (AR ~ 0.85) to demonstrate the computational results for this aspect ratio, and once validated, less scalable methods can be utilized to generate both higher aspect ratio structures and more complicated geometries/layering/hierarchy.

The present study provides a generalized thermal framework for the computational optimization of selective emitters for multiple applications. By introducing an optimized microscale pyramidal topology on the surface of nickel, alumina, and PDMS, selective anti-reflective behavior is induced that increases the absorptivity/emissivity of the surface. Optimized geometry for micropatterned nickel reaches a thermal solar absorption efficiency of 98.6%,

representing a dramatic increase from the ~35% solar absorption provided by untextured nickel. For alumina and PDMS, already excellent emission properties are enhanced significantly by inducing anti-reflective behavior in the MIR/NIR regions. This has the effect of increasing PDMS to near perfect blackbody emission in the MIR/NIR and alumina to an emission efficiency exceeding 91%. The pyramidal geometry has the benefit of being easily manufacturable, scalable, and can be patterned into all of the studied materials. A wide variety of geometric solutions induce significant anti-reflective behavior, indicating that precise fabrication requirements are not necessary to induce strongly absorbing behavior in these materials using this topology. Additionally, while the pyramidal design was studied thoroughly, the optimization framework provided is adaptable to any thermal emitter design that is compatible with the FDTD process. This method is easily expanded beyond the two-variable optimizations performed in this work. The results obtained will hopefully facilitate the development of a host of thermally optimized radiative heating and cooling designs.

Appendix A: Radiation Equations

$$E_{\lambda,b} = \pi I_{\lambda,b} = \frac{2hc_0^2\pi}{\lambda^5 \left(\exp\left(\frac{hc_0}{\lambda kT}\right)-1\right)} \tag{A1}$$

Where k is the Boltzmann constant, T is the temperature, h is the Planck constant, and c_0 is the speed of light in a vacuum. The total hemispherical power (radiated power), is calculated by integrating the wavelength dependent power over the specified wavelength range in all possible directions[41].

$$E = \int_0^\infty \int_0^{2\pi} \int_0^{\frac{\pi}{2}} I_{\lambda,e}(\lambda,\theta,\phi)\cos\theta\sin\theta \, d\theta d\phi d\lambda \tag{A2}$$

Which, when integrated, reduces the previous equation:

$$E_{\lambda,b} = \pi I_{\lambda,e}(\lambda) \tag{A3}$$

The above equations are considering a blackbody (where emissivity is unity through the spectrum), but for a non-unity emissivity, the integration for radiated power also varies with emissivity:

$$E_{\lambda,b} = \pi I_{\lambda,b} = \int_0^\lambda \frac{\varepsilon(\lambda,T)2hc_0^2\pi}{\lambda^5 \left(\exp\left(\frac{hc_0}{\lambda kT}\right)-1\right)} d\lambda \tag{A4}$$

Appendix B: Heat Transfer Balance for Surface Exposed to Atmospheric Window
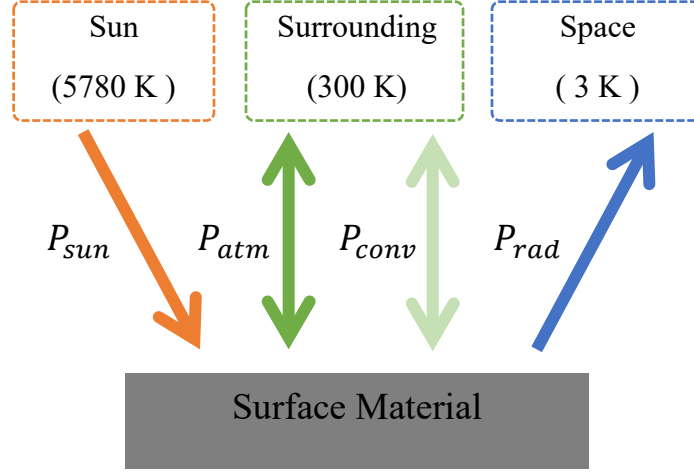
$$P_{net} = P_{rad} - P_{sun} - P_{atm} - P_{conv}$$

(Equations can be seen in Ref. [23], [26])

Here the overall net heat transfer balance and cooling equation are shown for a surface that is exposed to the ambient air, solar irradiation, and is open/exposed to the sky window. This equation can generally be used to describe available cooling power (P_{net}) for a fixed surface temperature or to solve for the temperature of the surface. The solar radiation term is expressed as:

$$P_{sun} = \int_0^\infty I_{AM1.5}(\lambda)\varepsilon(\lambda, T, \theta_{sun}) \cos\theta_{sun} d\lambda \tag{B1}$$

The radiation emitted from the surface is computed via an integration over the hemispherical emission area from the surface:

$$P_{rad} = \int \cos(\Omega) d\Omega \int_0^\infty I_{BB}(T, \lambda)\varepsilon(\lambda, T, \Omega) \, d\lambda \tag{B2}$$

Where and I_{BB} is expressed via Eqn. (A4) and the hemispherical term is expressed similar to Eqn. (A2), as:

$$\int d\Omega = \int_0^{\frac{\pi}{2}} \int_0^{2\pi} d\phi \sin\theta \, d\theta d\phi \qquad (B3)$$

The incident atmospheric radiation on the surface is computed in the exact same manner as Eqn. (A6), but accounts for atmospheric emission (ε_{atm}) in addition to the emissivity of the surface.

$$P_{rad} = \int \cos(\Omega) \, d\Omega \int_0^{\infty} I_{BB}(T,\lambda)\varepsilon(\lambda,T,\Omega)\varepsilon_{atm}(\lambda,\Omega) \, d\lambda \qquad (B4)$$

The emissivity of the atmosphere can be computed as a function of the transmission of the atmosphere (t) along the zenith,

$$\varepsilon_{atm}(\lambda,\Omega) = 1 - t(\lambda)^{\frac{1}{\cos\theta}} \qquad (B5)$$

The convective and conductive losses from the surface to its surroundings can be expressed using a combined "net heat transfer coefficient" (H_c). This value can generally be assumed to be near 10 W/m^{2}K for nominal conditions.

$$P_{conv} = H_c(T - T_{ambient}) \qquad (B6)$$

The system of equations are modified to generate the cost function equations shown in the work, but the shown heat transfer balance describes a general solution for radiative heating/cooling applications.

References

[1]   Purcell and Morin, *Electricity and Magnetism*, 3rd ed. New York: Cambridge University Press, 2013.

[2]   M. Planck, *The Theory of Heat Radiation*. Philidelphia, PA: P. Blakinston's Son & Co., 1914.

[3]   H. Eugene, *Optics*. Addison-Wesley, 2002.

[4]   Y. Wang, K. S. Chen, and S. C. Cho, *PEM Fuel Cells: Thermal and Water Management Fundamentals*. Momentum Press, 2013.

[5]   A. L. Fahrenbruch and R. . Bube, *Fundamentals of Solar Cells: Photovoltaic Solar Energy Conversion*. New York: Academic, 1983.

[6]   J. . Duffie and W. . Beckman, *Solar Thermal Engineering Processes*. New York: Wiley, 1980.

[7]   W. Stein and K. Lovegrove, Eds., *Concentrating Solar Power Technology: Principles, Developments and Applications*. Philidelphia, PA: Woodhead Publishing Limited, 2012.

[8]   T. J. Coutts, "Review of progress in thermophotovoltaic generation of electricity," *Renew. Sustain. energy Rev.*, vol. 3, no. 2, pp. 77–184, 1999, doi: 10.1016/S1364-0321(98)00021-5.

[9]   A. Lenert *et al.*, "A nanophotonic solar thermophotovoltaic device," *Nat. Nanotechnol.*, vol. 9, no. 2, pp. 126–130, 2014, doi: 10.1038/nnano.2013.286.

[10]   J. W. Schwede *et al.*, "Photon-enhanced thermionic emission for solar concentrator systems," *Nat. Mater.*, vol. 9, no. 9, pp. 762–767, 2010, doi: 10.1038/nmat2814.

[11]   S. D. Lord, "A New Software Tool for Computing Earth's Atmospheric Transmission of Near- and Far-Infrared Radiation," *NASA Tech. Memo. 103957*, no. December 1992, 1992.

[12]   M. M. Hossain and M. Gu, "Radiative cooling: Principles, progress, and potentials," *Adv. Sci.*, vol. 3, no. 7, pp. 1–10, 2016, doi: 10.1002/advs.201500360.

[13]   W. Li and S. Fan, "Nanophotonic control of thermal radiation for energy applications [Invited]," *Opt. Express*, vol. 26, no. 12, p. 15995, 2018, doi: 10.1364/oe.26.015995.

[14]   A. Erika, "The Persian Ice House, or How to Make Ice in the Desert," 2016. https://www.fieldstudyoftheworld.com/persian-ice-house-how-make-ice-desert/.

[15]   R. Kumar and M. A. Rosen, "Thermal performance of integrated collector storage solar water heater with corrugated absorber surface," *Appl. Therm. Eng.*, vol. 30, no. 13, pp. 1764–1768, 2010, doi: 10.1016/j.applthermaleng.2010.04.007.

[16]   N. Selvakumar, N. T. Manikandanath, A. Biswas, and H. C. Barshilia, "Design and fabrication of highly thermally stable HfMoN/HfON/Al 2O 3 tandem absorber for solar thermal power generation applications," *Sol. Energy Mater. Sol. Cells*, vol. 102, pp. 86–92, 2012, doi: 10.1016/j.solmat.2012.03.021.

[17]   H. W. Wang and L. W. Chen, "A cylindrical optical black hole using graded index photonic crystals," *J. Appl. Phys.*, vol. 109, no. 10, 2011, doi: 10.1063/1.3590336.

[18]   J. Qiu, L. H. Liu, and P. F. Hsu, "Radiative properties of optical board embedded with optical black holes," *J. Quant. Spectrosc. Radiat. Transf.*, vol. 112, no. 5, pp. 832–838, 2011, doi: 10.1016/j.jqsrt.2010.10.017.

[19]   J. Zhu, C. M. Hsu, Z. Yu, S. Fan, and Y. Cui, "Nanodome solar cells with efficient light management and self-cleaning," *Nano Lett.*, vol. 10, no. 6, pp. 1979–1984, 2010, doi: 10.1021/nl9034237.

[20] L. Zhou, X. Yu, and J. Zhu, "Metal-core/semiconductor-shell nanocones for broadband solar absorption enhancement," *Nano Lett.*, vol. 14, no. 2, pp. 1093–1098, 2014, doi: 10.1021/nl500008y.

[21] P. Li *et al.*, "Large-Scale Nanophotonic Solar Selective Absorbers for High-Efficiency Solar Thermal Energy Conversion," *Adv. Mater.*, vol. 27, no. 31, pp. 4585–4591, 2015, doi: 10.1002/adma.201501686.

[22] B. J. Lee, Y. Bin Chen, S. Han, F. C. Chiu, and H. J. Lee, "Wavelength-selective solar thermal absorber with two-dimensional nickel gratings," *J. Heat Transfer*, vol. 136, no. 7, pp. 1–7, 2014, doi: 10.1115/1.4026954.

[23] A. P. Raman, M. A. Anoma, L. Zhu, E. Rephaeli, and S. Fan, "Passive radiative cooling below ambient air temperature under direct sunlight," *Nature*, vol. 515, no. 7528, pp. 540–544, 2014, doi: 10.1038/nature13883.

[24] Y. Zhai *et al.*, "Scalable-manufactured randomized glass-polymer hybrid metamaterial for daytime radiative cooling," *Science (80-.).*, vol. 355, no. 6329, pp. 1062–1066, 2017, doi: 10.1126/science.aai7899.

[25] X. Nie, Y. Yoo, H. Hewakuruppu, J. Sullivan, A. Krishna, and J. Lee, "Cool White Polymer Coatings based on Glass Bubbles for Buildings," *Sci. Rep.*, vol. 10, no. 1, pp. 1–10, 2020, doi: 10.1038/s41598-020-63027-2.

[26] A. Krishna and J. Lee, "Morphology-Driven Emissivity of Microscale Tree-like Structures for Radiative Thermal Management," *Nanoscale Microscale Thermophys. Eng.*, vol. 22, no. 2, pp. 124–136, 2018, doi: 10.1080/15567265.2018.1446065.

[27] W. H. Southwell, "Antireflection Index Matching on Optical Surfaces," *J. Opt. Soc. Am. A*, vol. 8, no. 3, pp. 549–553, 1991.

[28] A. Deinega, I. Valuev, B. Potapkin, and Y. Lozovik, "Minimizing light reflection from dielectric textured surfaces," *J. Opt. Soc. Am. A*, vol. 28, no. 5, p. 770, 2011, doi: 10.1364/josaa.28.000770.

[29] T. Zhang, P. Zhang, S. Li, W. Li, Z. Wu, and Y. Jiang, "Black silicon with self-cleaning surface prepared by wetting processes," *Nanoscale Res. Lett.*, vol. 8, no. 1, pp. 1–5, 2013, doi: 10.1186/1556-276X-8-351.

[30] Y. Liu, A. Das, Z. Lin, I. B. Cooper, A. Rohatgi, and C. P. Wong, "Hierarchical robust textured structures for large scale self-cleaning black silicon solar cells," *Nano Energy*, vol. 3, pp. 127–133, 2014, doi: 10.1016/j.nanoen.2013.11.002.

[31] Y. J. Peng, H. X. Huang, and H. Xie, "Rapid fabrication of antireflective pyramid structure on polystyrene film used as protective layer of solar cell," *Sol. Energy Mater. Sol. Cells*, vol. 171, no. May, pp. 98–105, 2017, doi: 10.1016/j.solmat.2017.06.013.

[32] J. J. D. Leon, A. M. Hiszpanski, T. C. Bond, and J. D. Kuntz, "Design Rules for Tailoring Antireflection Properties of Hierarchical Optical Structures," *Adv. Opt. Mater.*, vol. 5, no. 13, pp. 1–8, 2017, doi: 10.1002/adom.201700080.

[33] P. Nagpal, N. C. Lindquist, S. H. Oh, and D. J. Norris, "Ultrasmooth patterned metals for plasmonics and metamaterials," *Science (80-.).*, vol. 325, no. 5940, pp. 594–597, 2009, doi: 10.1126/science.1174655.

[34] J. H. Park, P. Nagpal, K. M. McPeak, N. C. Lindquist, S. H. Oh, and D. J. Norris, "Fabrication of smooth patterned structures of refractory metals, semiconductors, and oxides via template stripping," *ACS Appl. Mater. Interfaces*, vol. 5, no. 19, pp. 9701–9708, 2013, doi: 10.1021/am402756d.

[35] "Finite Difference Time Domain (FDTD) solver introduction – Lumerical Support."

https://support.lumerical.com/hc/en-us/articles/360034914633-Finite-Difference-Time-Domain-FDTD-solver-introduction (accessed Jun. 03, 2020).

[36] H. Wang and L. Wang, "Perfect selective metamaterial solar absorbers," *Opt. Express*, vol. 21, no. S6, p. A1078, 2013, doi: 10.1364/oe.21.0a1078.

[37] D. L. C. Chan, M. Soljačić, and J. D. Joannopoulos, "Thermal emission and design in one-dimensional periodic metallic photonic crystal slabs," *Phys. Rev. E - Stat. Nonlinear, Soft Matter Phys.*, vol. 74, no. 1, pp. 206–214, 2006, doi: 10.1103/PhysRevE.74.016609.

[38] J. J. Shea, *Electronic materials and processes handbook, 3rd edition [Book Review]*, vol. 20, no. 5. 2004.

[39] E. D. Palik, *Handbook of Optical Constants of Solids*. Orlando: Academic Press, 1985.

[40] A. Srinivasan, B. Czapla, J. Mayo, and A. Narayanaswamy, "Infrared dielectric function of polydimethylsiloxane and selective emission behavior," *Appl. Phys. Lett.*, vol. 109, no. 6, 2016, doi: 10.1063/1.4961051.

[41] Incropera, DeWitt, Bergman, and Lavine, *Fundamentals of Heat and Mass Transfer*, 6th ed. John Wiley & Sons.

[42] C. A. Gueymard, D. Myers, and K. Emery, "Proposed reference irradiance spectra for solar energy systems testing," *Sol. Energy*, vol. 73, no. 6, pp. 443–467, 2002, doi: 10.1016/S0038-092X(03)00005-7.